

FREECORP™ 2.0

THEORETICAL BACKGROUND AND VERIFICATION

Prepared by:

Srdjan Nesic
Yougui Zheng
Ning Jing
Saba Navabzadeh Esmaeely
Zheng Ma

Athens, OH 45701
September 2018

PREFACE

Given the great popularity of FREECORP 1.0, which was launched in 2008, we are now releasing the second version, FREECORP™ 2.0, approximately a decade later. In the past 10 years, FREECORP 1.0 has been downloaded over 10,000 times by users from all over the world. This included students, professors, researchers, engineers, software developers and more. Since 2008, we have received feedback and suggestions from more than 250 users, ranging from corrosion industry experts to ambitious undergraduate students. FREECORP 1.0 has since been coupled and integrated with various other tools such as those for: multi-phase flow prediction, process design, computational fluid dynamics (CFD), etc. It is worth remembering that part of the success was related to the fact that FREECORP 1.0 was based on clear theoretical foundations, was fully transparent, it relied exclusively on information in the public domain and that the background behind the models was fully shared with the users. After ten years, we feel that we have realized our initial goal – to bring the best possible tool that can help understand and predict corrosion of mild steel in aqueous systems containing CO₂, H₂S, and organic acids, typical for oil and gas applications, to the broadest possible audience – and make it available – for free.

This is not to say that FREECORP 1.0 was without problems. Apart from the few bugs that were discovered and fixed early on, we realized through feedback provided by the users, that there are features that we could have implemented better and others that were missing altogether, what sparked new ideas and inspired us to continue working on them. Moreover, our understanding of the physicochemical phenomena underlying this type of corrosion has improved significantly over the past decade and we wanted to bring all that back to the FREECORP community. This has led us to development of FREECORP™ 2.0.

In many ways, FREECORP™ 2.0 was built with the same goals and approach in mind as its predecessor. We still wanted to reach the broadest possible audience, offer them models based on best possible science, present the theoretical background as clearly and as competently as we can, verify the model performance with most accurate empirical data, deliver the models via software that is easy to use and flexible, and keep it all – free. Time ahead will tell if we were successful in this quest.

While this document outlines the theory behind FREECORP™ 2.0, in some detail, it is worth highlighting here some of main improvements over FREECORP 1.0.

- the two main models covering electrochemical corrosion of mild steel due to aqueous CO₂ and H₂S are now seamlessly integrated with each other and the organic acid corrosion model;
- in addition to the steady-state electrochemical corrosion model featured in FREECORP 1.0, there is a fully mechanistic transient corrosion model in FREECORP™ 2.0 that covers formation and protection by corrosion product layers;
- the model for calculating water speciation was significantly improved;
- one can now use the new intuitive user interface or work with FREECORP™ 2.0 directly by connecting to it from other applications and programming environments.

We hope that the new FREECORP™ 2.0 will be at least as useful and popular as its predecessor. Either way, we are fully committed to supporting it and making it even better in the years to come.

S. Nesić
Athens OH
September 2018

TABLE OF CONTENTS

Chapter 1. INTRODUCTION	7
Chapter 2. AQUEOUS CHEMISTRY	8
2.1 Aqueous Chemistry in the Presence of CO ₂	9
2.2 Aqueous Chemistry in the Presence of H ₂ S.....	14
2.3 Aqueous Chemistry in the Presence of Both CO ₂ and H ₂ S	17
2.4 Aqueous Chemistry in the Presence of Organic Acids	18
Chapter 3. STEADY STATE MODEL	21
3.1 Strong Acid Environment	21
3.1.1 Cathodic Reactions	22
3.1.2 Anodic Reaction.....	26
3.1.3 The Mixed Potential Theory	28
3.1.4 Model Verification.....	28
3.2 Aqueous CO ₂ Environment.....	30
3.2.1 Cathodic Reaction.....	30
3.2.2 Anodic Reaction.....	31
3.2.3 The Mixed Potential Theory	32
3.2.4 Model Verification.....	33

3.3 Aqueous H ₂ S Environment	35
3.3.1 Cathodic Reactions	35
3.3.2 Anodic Reaction.....	38
3.3.3 The Mixed Potential Theory	39
3.3.4 Model Verification.....	40
3.4 Mixed CO ₂ / H ₂ S Environment.....	53
3.4.1 Cathodic Reactions	53
3.4.2 Anodic Reaction.....	53
3.4.3 The Mixed Potential Theory	54
3.4.4 Model Verification.....	54
3.5 Aqueous Environment in the Presence of Organic Acids.....	62
3.5.1 Cathodic Reactions	62
3.5.2 Anodic Reaction.....	64
3.5.3 The Mixed Potential Theory	64
3.5.4 Model Verification.....	64
3.6 Model Limitations.....	65
Chapter 4. TRANSIENT MODEL	67
4.1 Iron Carbonate and Iron Sulfide	67
4.2 Model Construction	70

4.2.1	Bulk Water Chemistry Model	70
4.2.2	Electrochemical Corrosion Model	71
4.2.3	Corrosion Product Layer Growth Model	79
4.3	Model Verification.....	87
4.3.1	Verification of Model without Corrosion Product Layer	87
4.3.2	Verification of Model in Iron Sulfide Layer Forming Conditions ...	88
4.4	Model Limitations.....	94
	References	95

CHAPTER 1. INTRODUCTION

As the oil and gas emerge from the geological formation, they are always accompanied by some water and varying amounts of “acid gases”: carbon dioxide, CO₂, hydrogen sulfide, H₂S, and organic acids. This is a corrosive combination that affects the integrity of mild steel. Even if this has been known for over 100 years, aqueous CO₂/H₂S/organic acid corrosion of mild steel still represents a significant problem for the oil and gas industry. Although corrosion resistance alloys exist that are able to withstand this type of corrosion, mild steel is still the most cost effective construction material used in this industry for these applications. All of the pipelines, many wells and much of the processing equipment in the oil and gas industry are built out of mild steel. The cost of equipment failure due to internal CO₂/ H₂S corrosion is enormous, both in terms of direct costs such as: repair costs and lost production, as well as in indirect costs such as: environmental cost, impact on the downstream industries, etc. The text below summarizes the degree of understanding of the so-called “sweet” CO₂ corrosion, the so-called “sour” or H₂S corrosion, and organic acid corrosion of mild steel exposed to aqueous environments. It also casts the knowledge in the form of mathematical equations used to construct mechanistic models, built into FRECCORP 2.0., which should enable corrosion engineers and scientists to predict the rate and mechanisms of corrosion attack.

FREECORP™ 2.0 package has two main sub-models. The first one is the “steady state” electrochemical corrosion model that does not include formation of protective corrosion product layers on the steel surface, and all calculations are based on the bulk water chemistry parameters. It is similar in approach and appearance to the

electrochemical model of CO₂ corrosion built previously into FREECORP 1.0. The main difference is that the new electrochemical model built into FREECORP™ 2.0 accounts for H₂S in the similar fashion as is done for CO₂, what was not the case in FREECORP 1.0, where the H₂S corrosion model was not electrochemical in nature and was therefore quite different from the CO₂ corrosion model.

The other sub-model built into FREECORP™ 2.0 is the transient electrochemical model that accounts for formation of corrosion product layers: iron carbonate in CO₂ containing solutions and/or iron sulfide in H₂S containing solutions. The calculations in this model are based on surface water chemistry conditions. To some extent it is similar to the H₂S corrosion model built into FREECORP 1.0, except for the fact that is more comprehensive in approach and scope, as explained further below in the text.

In the text below, the basic model used to obtain water speciation in FREECORP™ 2.0 is explained first. This is followed by the description of the model of the electrochemical reactions which is the underpinning of both the steady state and the transient corrosion models in FREECORP™ 2.0. Finally, the model for corrosion product layer growth is presented (both for iron carbonate and iron sulfide), which is implemented in the transient model of FREECORP™ 2.0.

CHAPTER 2. AQUEOUS CHEMISTRY

The aqueous chemistry described in this chapter is based on a simple equilibrium model of an ideal aqueous solution, based on the so called “infinite dilution theory”. This bulk water chemistry model forms a base for the electrochemical model built into FREECORP™ 2.0, described in the following chapter.

2.1 Aqueous Chemistry in the Presence of CO₂

Dry CO₂ gas is not corrosive, but when it dissolves in water, a series of chemical reactions occur, and that may make the resultant solution corrosive to mild steel. These reactions have been listed in Table 1 and are taken into consideration in FREECORP 2.0 in order to calculate species concentrations at different conditions¹⁻³. The equations for calculating the equilibrium constants are given in Table 2 below.

Table 1. Main chemical reactions occurring in an aqueous CO₂ solution and corresponding equilibrium expressions

Name	Homogenous chemical reaction		Equilibrium expression
CO ₂ dissolution	CO _{2(g)} ⇌ CO _{2(aq)}	(1)	$K_{sol} = \frac{c_{CO_2}}{pCO_2}$ (2)
CO ₂ hydration	CO _{2(aq)} + H ₂ O _(l) ⇌ H ₂ CO _{3(aq)}	(3)	$K_{hyd} = \frac{c_{H_2CO_3}}{c_{CO_2}}$ (4)
Carbonic acid dissociation	H ₂ CO _{3(aq)} ⇌ H ⁺ _(aq) + HCO ₃ ⁻ _(aq)	(5)	$K_{ca} = \frac{c_{HCO_3^-} c_{H^+}}{c_{H_2CO_3}}$ (6)
Bicarbonate ion dissociation	HCO ₃ ⁻ _(aq) ⇌ H ⁺ _(aq) + CO ₃ ²⁻ _(aq)	(7)	$K_{bi} = \frac{c_{CO_3^{2-}} c_{H^+}}{c_{HCO_3^-}}$ (8)
Water dissociation	H ₂ O _(l) ⇌ H ⁺ _(aq) + OH ⁻ _(aq)	(9)	$K_{wa} = c_{H^+} c_{OH^-}$ (10)

* Subscript “g” stands for gas phase. “aq” stands for aqueous phase. “l” stands for liquid. In the following text, if not specifically indicated, CO₂ and H₂S are always referring to the amount in the aqueous phase, even if we do not use the “aq” subscript. All the concentrations in this chapter refer to equilibrium conditions, however, the subscript “eq” was not used to keep the expressions simple.

Table 2. The empirical equations for the equilibrium constants

$$K_{sol} = \frac{14.5}{1.00258} \times 10^{-(2.27 + 5.65 \times 10^{-3}T_f - 8.06 \times 10^{-6}T_f^2 + 0.075I)} \text{ molar/bar} \quad (11)^4$$

$$K_{hyd} = 2.58 \times 10^{-3} \quad (12)^5$$

$$K_{ca} = 387.6 \times 10^{-\left(6.41 - 1.594 \times 10^{-3}T_f + 8.52 \times 10^{-6}T_f^2 - 3.07 \times 10^{-5}p - 0.4772I^{\frac{1}{2}} + 0.118I\right)} \text{ molar} \quad (13)^4$$

$$K_{bi} = 10^{-(10.61 - 4.97 \times 10^{-3}T_f + 1.331 \times 10^{-5}T_f^2 - 2.624 \times 10^{-5}p - 1.66I^{\frac{1}{2}} + 0.34661I)} \text{ molar} \quad (14)^4$$

$$K_{wa} = 10^{-(29.3868 - 0.0737549T_k + 7.47881 \times 10^{-5}T_k^2)} \text{ molar}^2 \quad (15)^6$$

* T_f is temperature in degrees Fahrenheit, T_k is absolute temperature in Kelvin, I = $\frac{1}{2} \sum_i c_i z_i^2$ is ionic strength in molar, and p is the pressure in bar.

To calculate the bulk concentrations of all these species, and the solution pH, in an aqueous CO₂ solution, a water chemistry model can be constructed. For a so-called “open system”, the *pCO₂* can be considered to be constant and treated as a known variable. A lab example is a glass-cell system with continuous purging of gaseous CO₂, at a constant pressure. In the field, an example would be a wet gas transportation line with some liquid water present, where the amount of gaseous CO₂ is much larger relative to that dissolved in water. In either of the cases it is assumed that change in the amount of CO₂ dissolved in water does not affect the amount of CO₂ in the gas phase.

Therefore, for an open system, referring to Table 1 and Table 2, there are 6 unknown aqueous concentrations of species in solution (CO₂, H₂CO₃, HCO₃⁻, CO₃²⁻, OH⁻, H⁺). Five equations relating to the equilibrium expressions are listed in Table 2. One more equation is needed to determine the species concentration in an aqueous CO₂ solution. Since the aqueous solution is always charge-neutral, the electro-neutrality equation can be used to reflect this, as equation (16) shows:

$$c_{H^+} = c_{HCO_3^-} + 2c_{CO_3^{2-}} + c_{OH^-} \quad (16)$$

Equation (16) is valid only for a pure, CO₂-saturated aqueous solution in the absence of other species. If other ions, such as for example Fe²⁺, Cl⁻, Na⁺, etc., are present in the aqueous solution, then Equation (16) can be adjusted to include these species, as Equation (17) shows.

$$c_{H^+} + 2c_{Fe^{2+}} + c_{Na^+} = c_{HCO_3^-} + 2c_{CO_3^{2-}} + c_{OH^-} + c_{Cl^-} \quad (17)$$

The solution pH is often observed to increase in lab corrosion tests, particularly for a small volume autoclave or glass cell, due to the release of Fe^{2+} from the dissolution of iron in mild steel, thereby perturbing the distribution of the ionic species given by Equation (17). Dilute hydrochloric acid (HCl) or sodium hydroxide (NaOH) solutions are often used to adjust the pH of the solution without introducing additional species; the addition of excess Na^+ (provided by NaOH) or Cl^- (provided by HCl) will change the charge balance of species, as shown by Equation (17), and affect all species concentrations.

If additional homogeneous reactions occur, and/or additional species are introduced, the appropriate reaction equilibrium expressions need to be added to those shown above, as would be the case for H_2S addition, and organic acid addition, described further below.

An example of a calculated CO_2 aqueous species distribution as a function of pH for an open system is given in Figure 1. Clearly the concentration of dissolved CO_2 and H_2CO_3 do not change with pH due to partial pressure of CO_2 which is assumed to be constant.

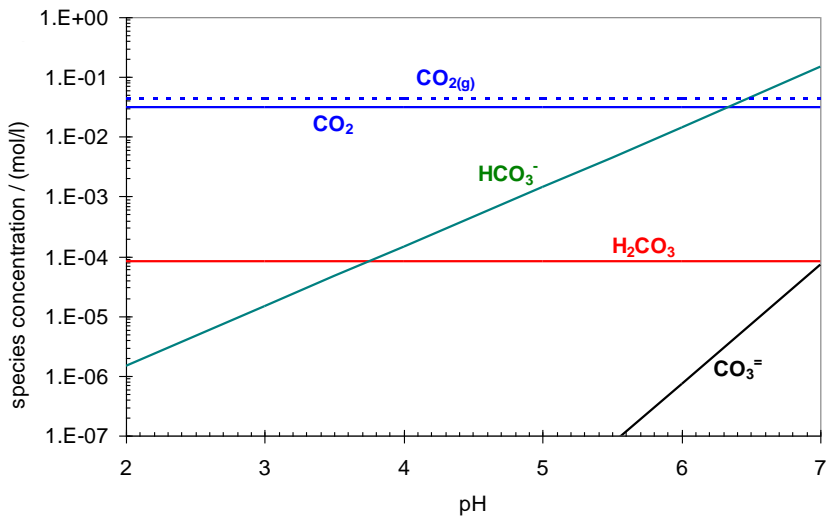


Figure 1. Carbonic species concentrations as a function of pH for a CO_2 saturated aqueous solution at $\text{PCO}_2=1$ bar, 25°C , 1wt% NaCl.

The corrosion models in FREECORP™ 2.0 are based on the “open system” water chemistry model, as described above.

The situation is different in a “closed system” where the amount of gaseous CO_2 is limited, such as in an autoclave test or in an oil line with a small gas phase. There, the pressure of gaseous CO_2 cannot be any longer considered to be constant and known in advance, since it will change as other conditions and aqueous concentrations change. Based on the simple water chemistry model presented above, the additional unknown ($p\text{CO}_2$) requires an additional equation to calculate it. For a closed system, we can use the conservation equation for CO_2 species, i.e. assume that the total amount of aqueous carbonic species (expressed in moles) is constant, as shown in (18):

$$N_{\text{CO}_2(\text{g})} + N_{\text{CO}_2(\text{aq})} + N_{\text{H}_2\text{CO}_3} + N_{\text{HCO}_3^-} + N_{\text{CO}_3^{2-}} = \text{constant} \quad (18)$$

The concentrations of different species in both the gas phase and the aqueous solution can then be calculated based on Equations (2) to (18) for a closed system.

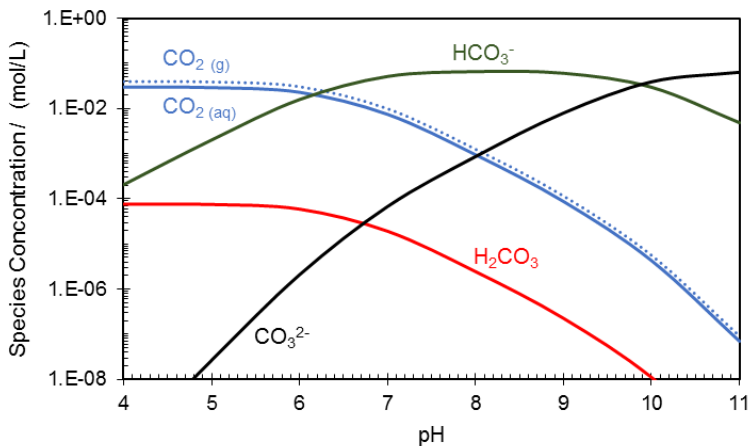


Figure 2. Carbonic species concentrations as a function of pH for a closed system, gas volume / liquid volume =1:1, initial p_{CO_2} =1 bar, 1wt%NaCl and 25°C.

In applications, the pH is not known and is a function of the CO_2 partial pressure (amongst other factors). The pH decreases with increasing CO_2 partial pressure, as dissolved CO_2 acidifies the solution by carbonic acid dissociation. The pH of the solution is very important as the hydrogen ion is a species involved in the cathodic reactions at the steel surface; the lower the pH, the more corrosive the solution is, and *vice versa*. The calculated pH of pure water and water with 3% NaCl as a function of p_{CO_2} at room temperature is shown in

Figure 3. Another significance of pH and CO_2 partial pressure is that they impact the formation of iron carbonate corrosion product layers, by affecting the saturation of iron carbonate, described in more detail below.

In summary, the water speciation changes due to the presence of CO_2 in an aqueous system. The pH can be readily calculated at equilibrium, along with concentrations of all other species, which affect the corrosion process.

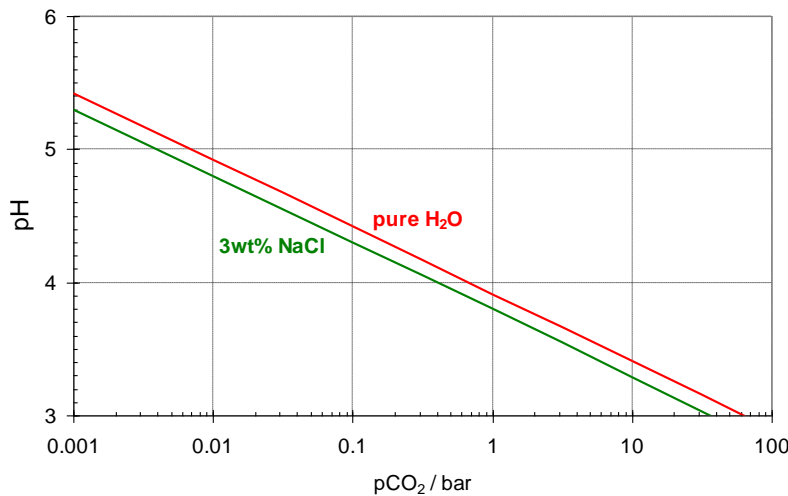


Figure 3. pH of a pure aqueous solution saturated with CO₂ as a function of the partial pressure of CO₂; T=25°C, 1wt% NaCl.

2.2 Aqueous Chemistry in the Presence of H₂S

Similar to the CO₂ case, aqueous H₂S is a weak acid and can partially dissociate to produce H⁺ ions. At low pressure, the solubility of H₂S gas can be calculated by Henry's law. The chemical reactions occurring in the bulk solution and corresponding equilibrium expressions are listed in Table 3. Many studies have been conducted to elucidate the thermodynamics of H₂S water chemistry⁸. The equations for calculating equilibrium constants used in FRECCORP 2.0 are given in Table 4.

Table 3. Key chemical reactions in aqueous H₂S solution and corresponding equilibrium expressions

Name	Homogenous chemical reaction	Equilibrium expression
H ₂ S gas dissolution	$\text{H}_2\text{S}_{(\text{g})} \rightleftharpoons \text{H}_2\text{S}_{(\text{aq})}$ (19)	$K_{\text{sol(H}_2\text{S)}} = \frac{c_{\text{H}_2\text{S}}}{p_{\text{H}_2\text{S}}}$ (20)
H ₂ S dissociation	$\text{H}_2\text{S}_{(\text{aq})} \rightleftharpoons \text{H}_{(\text{aq})}^+ + \text{HS}_{(\text{aq})}^-$ (21)	$K_{hs} = \frac{c_{\text{HS}^-} c_{\text{H}^+}}{c_{\text{H}_2\text{S}}}$ (22)
HS ⁻ ion dissociation	$\text{HS}_{(\text{aq})}^- \rightleftharpoons \text{H}_{(\text{aq})}^+ + \text{S}_{(\text{aq})}^{2-}$ (23)	$K_{bs} = \frac{c_{\text{S}^{2-}} c_{\text{H}^+}}{c_{\text{HS}^-}}$ (24)

Table 4. The empirical equations for the equilibrium constants

$$K_{sol(H_2S)} = 10^{-(634.27 + 0.2709 T_k - 0.00011132 T_k^2 - 16719/T_k - 261.9 \log_{10} T_k)} \quad (25)^9$$

molar/bar

$$K_{hs} = 10^{782.43945 + 0.36126 T_k - 0.00016722 T_k^2 - 20565.7315/T_k - 142.7417222 \log(T_k)} \quad (26)^9$$

molar

$$K_{bs} = 10^{(-23.93 + 0.030446 * T_k - 2.4831 * 10^{-5} * T_k^2)} \text{ molar} \quad (27)^6$$

For a pure H₂S system, the concentration of different sulfide species can be calculated by a water chemistry model similar to that shown above for a CO₂ aqueous environment. In an open system, there are 5 variables for the concentration of species (H⁺, OH⁻, H₂S, HS⁻, S²⁻), which are found in the 4 equilibrium expressions in Table 3 and Table 4. The new electroneutrality equation is:

$$c_{H^+} = c_{HS^-} + 2c_{S^{2-}} + c_{OH^-} \quad (28)$$

In a closed system, an additional unknown variable, pH₂S, needs to be accounted for. The total amount of sulfide species (in moles) is conserved, given in Equation (29) below:

$$N_{H_2S(g)} + N_{H_2S(aq)} + N_{HS^-} + N_{S^{2-}} = constant \quad (29)$$

Figure 4 shows an example of equilibrium distribution of sulfide species changing with pH at 1bar, 25°C, by employing the open system model. If the closed system model is applied, the distribution of equilibrium sulfide species changing with pH is shown in Figure 5.

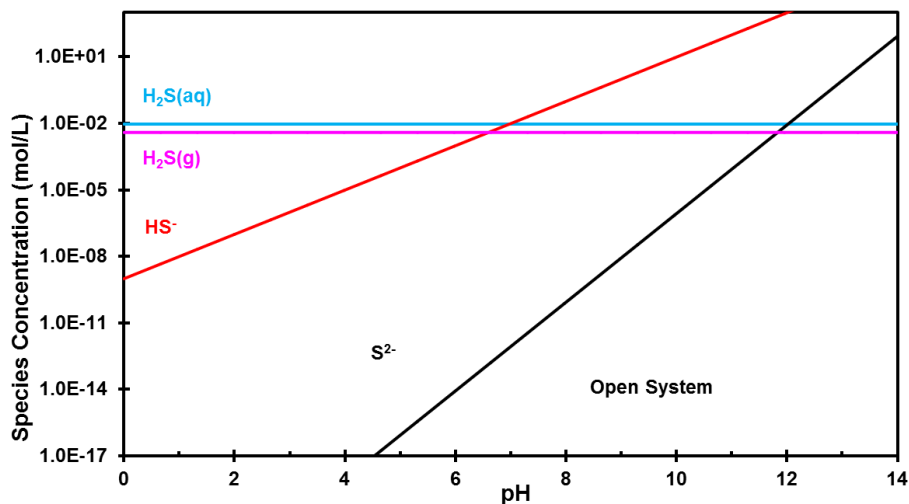


Figure 4. Equilibrium concentration of sulfide species as a function of pH for an open system at $\text{pH}_2\text{S} = 0.1$ bar and 25°C .

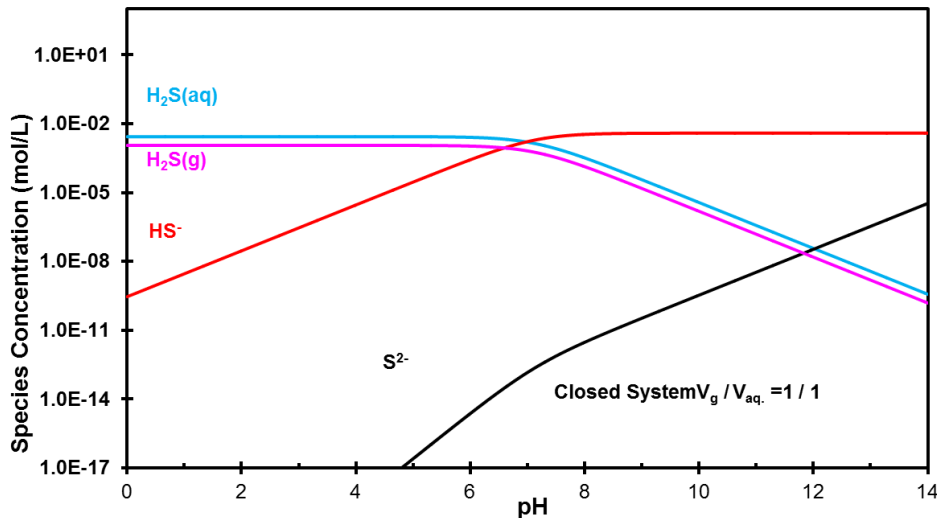


Figure 5. Equilibrium concentration of sulfide species as a function of pH for a closed system at gas volume / liquid volume = 1:1 and initial $\text{pH}_2\text{S} = 0.1$ bar and 25°C .

From Table 3 and Table 4, it can be seen that the fundamental difference between the CO_2 and the H_2S water chemistry is that the aqueous CO_2 must undergo a hydration step to form H_2CO_3 before dissociation while aqueous H_2S can directly dissociate

following dissolution. H_2CO_3 concentration can be calculated by $c_{\text{H}_2\text{CO}_3} = K_{\text{sol}}K_{\text{hyd}} * p\text{CO}_2$ based on Equations (2) and (4). Aqueous H_2S concentration can be calculated using $c_{\text{H}_2\text{S}} = K_{\text{sol}(\text{H}_2\text{S})} * p\text{H}_2\text{S}$. Over the range of 20°C to 80°C, the ratio between $K_{\text{sol}}K_{\text{hyd}}$ for the CO_2 system and $K_{\text{sol}(\text{H}_2\text{S})}$ at the different temperatures is shown in Table 5, which is of the order of 1000. This indicates that the concentration of aqueous H_2S concentration will be about 1000 times higher than aqueous H_2CO_3 concentration at the same partial pressures of CO_2 or H_2S gas. In other words, in a 1 bar $p\text{CO}_2$ system the concentration of aqueous H_2CO_3 is of the same order of magnitude as the concentration of aqueous H_2S when the pH_2S is about 1 mbar (1000 ppm at 1 bar total pressure). This type of number is often used as an argument to decide whether corrosion is sweet or sour, i.e. whether it is “dominated” by CO_2 or H_2S , although such designations are often misleading.

Table 5. The ratio between $K_{\text{sol}} * K_{\text{hyd}}$ and $K_{\text{sol}(\text{H}_2\text{S})}$

Tc(°C)	20	40	60	80
$K_{\text{sol}} * K_{\text{hyd}}$ (molar/bar)	9.0×10^{-5}	6.3×10^{-5}	4.7×10^{-5}	3.6×10^{-5}
$K_{\text{sol}(\text{H}_2\text{S})}$ (molar/bar)	1.1×10^{-1}	6.9×10^{-2}	5.0×10^{-2}	4.0×10^{-2}
Ratios of $K_{\text{sol}(\text{H}_2\text{S})}$ with $K_{\text{sol}} * K_{\text{hyd}}$	1.2×10^3	1.1×10^3	1.1×10^3	1.1×10^3

2.3 Aqueous Chemistry in the Presence of Both CO_2 and H_2S

One can combine the equations shown in Table 1, Table 2, Table 3, and Table 4 to calculate the pH and the distribution of species in a mixed $\text{CO}_2/\text{H}_2\text{S}$ aqueous system. Figure 6 shows an example of equilibrium concentrations as a function of pH for a mixed $\text{CO}_2/\text{H}_2\text{S}$ open system. The concentration of aqueous H_2S is almost the same as the concentration of H_2CO_3 . However, the concentration of HS^- is much smaller than the

HCO_3^- concentration when the concentrations of H_2CO_3 and H_2S are the same because the dissociation constant for H_2S is 500 to 2000 times smaller than that for H_2CO_3 , which also means that the H^+ release from aqueous H_2S is also much smaller. At the same gaseous pressure of H_2S and CO_2 (for example, 1 bar), the concentration of aqueous H_2S concentration is much higher (almost 1000 times higher) than aqueous H_2CO_3 concentration, but the resulting pH is almost the same in both conditions due to the lower dissociation constant for H_2S .

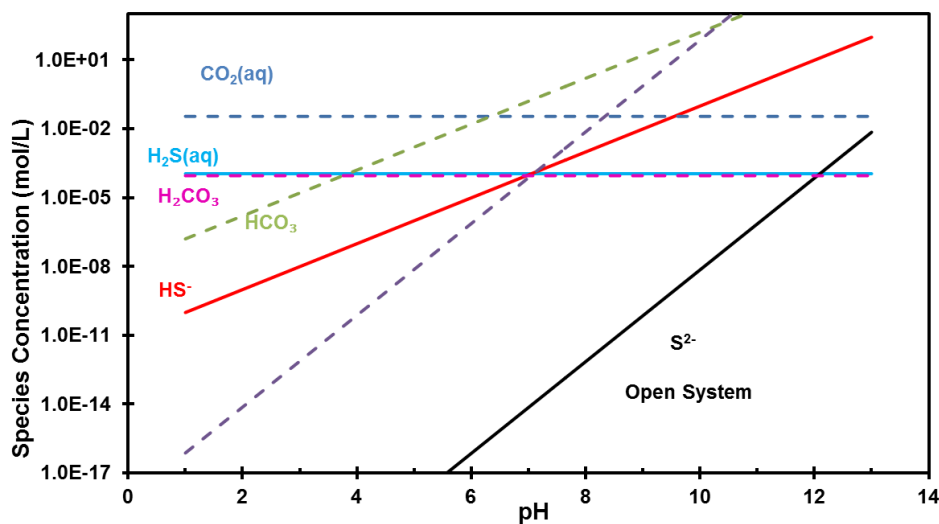
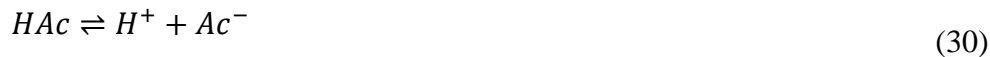


Figure 6. Equilibrium concentrations of different species as a function of pH for a mixed $\text{CO}_2/\text{H}_2\text{S}$ open system.

2.4 Aqueous Chemistry in the Presence of Organic Acids

When organic acids are present, even at concentrations as low as 100 ppm, this can cause severe corrosion of mild steel. A number of low molecular weight, water soluble, organic/carboxylic acids are found in oilfield brines, such as formic acid (HCOOH) and propionic acid ($\text{CH}_3\text{CH}_2\text{COOH}$), etc., however acetic acid (CH_3COOH or shortly HAc) is by far the most prevalent organic acid causing corrosion problems for mild steel. The

detrimental effect of acetic acid was primarily seen at high temperatures ($>50^{\circ}\text{C}$) and in the lower pH range (pH 3.5-5.0). Similar to aqueous H_2CO_3 and H_2S , the HAc is also a weak – partially dissociated acid, according to Reaction (30).



The equilibrium constant for dissociation of HAc is a function of temperature and can be calculated as:

$$K_{\text{HAc}} = 10^{-(6.66104 - 0.0134916 \cdot T_K - 2.37856 \cdot 10^{-5} T_K^2)} \quad (31)$$

The pH, determines the distribution of the acetic species in the solution, as shown in Table 6 for a typical pH range of oilfield brines. Clearly, at pH 4, corresponding to a pure water/ CO_2 system seen for example in condensed water, most of the acetic species are in the form of undissociated acid. The opposite is true at pH 6.6, typical for heavily buffered brines, where most of the acetic species are in the form of acetate ion.

Table 6. Acetic acid species distribution at various pH values (at 80°C).

pH	$c_{\text{HAc}} / \text{mol \%}$	$c_{\text{Ac}^-} / \text{mol \%}$
4	88	12
5	42	58
6	6.8	93.2
6.6	1.8	98.2

The aqueous speciation can be found by solving the equilibrium expressions presented above. The concentrations of some of the key species at 1 bar CO₂, 22°C when 10 ppm HAc (total) is added as shown in

Figure 7. The concentration of dissolved carbon dioxide and carbonic acid is fixed with the partial pressure of the gas and is not a function of pH. It is evident that when 10 ppm HAc is added to the solution, HAc is the main source of acidity up to a pH of approximately 4.7. When 100 ppm HAc is added, under the same conditions, it is the main source of acidity up to a pH of almost 6. This is shown in

Figure 8.

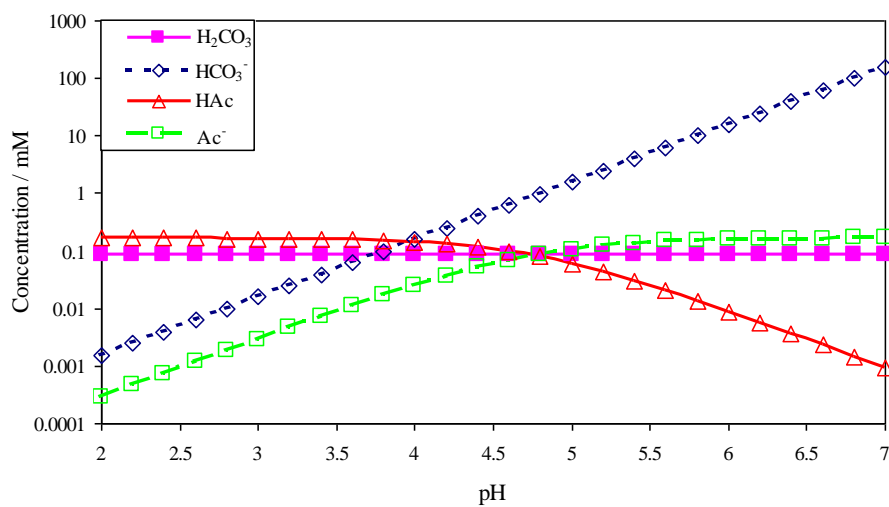


Figure 7. The effect of pH on the concentration of species at 1 bar CO₂, 22°C when 10 ppm HAc is present.

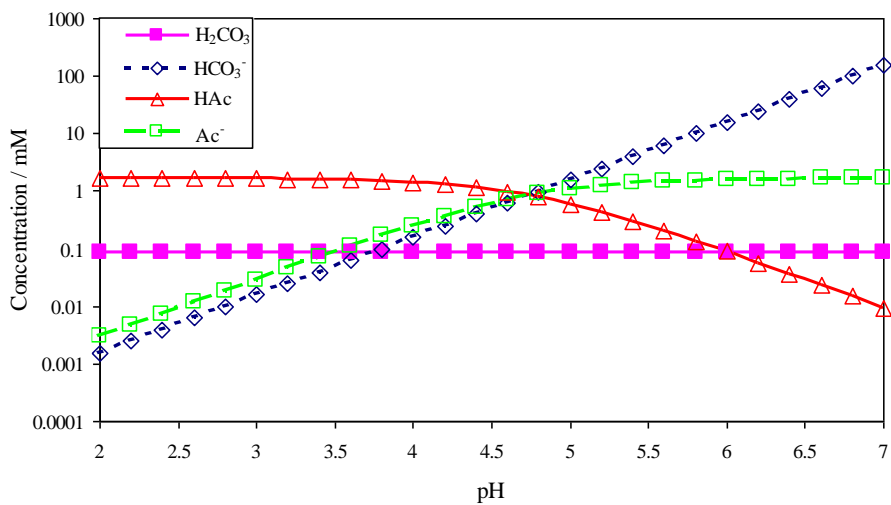


Figure 8. The effect of pH on the concentration of species at 1 bar CO_2 , 22°C when 100 ppm HAc is present.

CHAPTER 3. STEADY STATE MODEL

The electrochemical corrosion model built into FREECORPTM 2.0 that is described in this section is a steady state model based on bulk water chemistry conditions (as calculated using the model presented in the previous section). It does not include the formation of any kind of surface corrosion product layers, and does not account for their protectiveness. This issue is dealt with in the following chapter.

3.1 Strong Acid Environment

The description of electrochemical reactions underlying corrosion will first be presented for the simplest case of mild steel corroding in a so called “strong” acid aqueous environment (in the absence of CO_2 and H_2S). The chemical designation of a “strong” acid here refers to a case where the acid is practically fully dissociated when in water, such as is the case for example with aqueous HCl. It does not imply a very low pH (at least not in our case), and actually in the examples discussed below, the pH is

typically in the mildly acidic to near neutral range of pH 3 – pH 7. When CO₂ and/or H₂S are present in the system, this is often referred to as corrosion of mild steel in “weak” acid aqueous solutions, really suggesting only that the dissociation of the aqueous acids (H₂CO₃ and H₂S) in these system is only partial, as described further below. The word “weak” does not imply a low corrosion rate either, actually corrosion in “weak” CO₂ and/or H₂S aqueous solutions is often more severe than in “strong” acids at the same pH.

3.1.1 Cathodic Reactions

When H₂S or CO₂ are not present in the water, the main cathodic reaction is hydrogen evolution *via* the reduction of H⁺ ions:



This is the most important cathodic reaction in acidic solutions. In the case of mild steel corrosion, this reaction is usually limited by the mass transport rate of H⁺ ions from the bulk solution to the steel surface (mass transfer limitation).

As the availability of H⁺ ions decreases, in more neutral solutions (typically pH > 6), hydrogen evolution via the direct reduction of water may become important:



For H⁺ reduction, in order to describe the effect of charge transfer and mass transfer on H⁺ reduction, the current density for reduction of H⁺ can be thought of as consisting of two components: charge transfer current and mass transfer limiting current is calculated using the equation below¹:

$$\frac{1}{i_{H^+}} = \frac{1}{i_{\alpha,H^+}} + \frac{1}{i_{\text{lim},H^+}^d} \quad (34)$$

where i_{H^+} is total current density of H^+ reduction (A/m^2), i_{α,H^+} is the charge transfer current density (A/m^2), and i_{lim,H^+}^d is the diffusion limiting current density.

The charge transfer current density can be calculated using the Tafel equation as:

$$i_{\alpha,H^+} = i_{0,H^+} \times 10^{-\frac{\eta}{b_c}} \quad (35)$$

where i_{0,H^+} is the exchange current density (A/m^2), b_c is the cathodic Tafel slope (V/decade), η is the over potential (V), which is equal to the difference between the operating (actual) potential and the reversible potential.

The cathodic Tafel slope b_c can be calculated from:

$$b_c = \frac{2.303RT}{\alpha_c F} \quad (36)$$

According to Bockris, *et al.*¹⁰, for H^+ reduction, $\alpha_c = 0.5$ giving $b_c \approx 0.120$ V/decade at 30°C.

The reversible potential of hydrogen reduction can be calculated as:

$$E_{rev(H^+)} = -\frac{2.303RT}{F} pH - \frac{2.303RT}{2F} \log p_{H_2} \quad (37)$$

where the partial pressure of hydrogen normally is assumed to be close to zero. The only unknown model parameter for calculating the charge transfer current density is the exchange current density, i_{0,H^+} . According to Nešić *et al.*¹¹ i_{0,H^+} can be calculated by:

$$i_{0,H^+} = i_0^{ref} \left(\frac{c_{H^+}}{c_{H^+ ref}} \right)^{0.5} \times e^{-\frac{\Delta H}{R} \left(\frac{1}{T} - \frac{1}{T_{ref}} \right)} \quad (38)$$

where i_0^{ref} is the reference exchange current density at a reference temperature, T_{ref} (K) and reference concentration of H^+ . ΔH is the enthalpy of activation for the H^+ reduction reaction (J/mol).

The i_0^{ref} for H^+ reduction was taken as 0.03 A/m^2 at a reference temperature of 20°C and reference H^+ concentration of $1\times 10^{-4} \text{ mol/L}$. The enthalpy of activation was taken as 30 kJ/mol^{12} . No effect of H_2S on H^+ reduction was found in our experiments.

The diffusion limiting current in Equation (34) is calculated with:

$$i_{\lim,H^+}^d = k_{m,H^+} F c_{H^+} \quad (39)$$

where k_{m,H^+} represents H^+ mass transfer coefficient (m/s) and c_{H^+} represents the bulk concentration of H^+ (mol/m^3).

The mass transfer coefficient of H^+ can be calculated from correlations, e.g. from a rotating cylinder correlation described by Eisenberg *et al.*¹²

$$Sh = \frac{k_{m,H^+} d_{RCE}}{D_{H^+}} = 0.0791 \times Re^{0.7} \times Sc^{0.356} \quad (40)$$

where Sh is Sherwood number; d_{RCE} : pipe diameter (m); D_{H^+} is diffusion coefficient of hydrogen ion (m^2/s); Re is Reynolds number = $\rho u d_{RCE} / \mu$; and Sc is Schmidt number = $\mu / \rho D_{H^+}$.

For the case of pipe flow the mass transfer coefficient in turbulent single phase flow can be calculated by a straight pipe correlation of Berger and Hau¹³:

$$Sh = 0.0165 \times Re^{0.86} \times Sc^{0.33} \quad (41)$$

For different geometries, the appropriate mass transfer coefficient should be used.

The diffusion coefficient of species in a dilute solution can be calculated by the Stokes-Einstein equation below

$$D_{H^+} = D_{ref(H^+)} \times \frac{T_k}{T_{ref}} \times \frac{\mu_{ref}}{\mu} \quad (42)$$

where $D_{ref(H^+)}$ represents the reference diffusion coefficient at a reference temperature, and was taken as $9.31 \times 10^{-9} \text{ m}^2/\text{s}$ ¹⁴. μ represents the water viscosity in $\text{kg}/\text{m}\cdot\text{s}$ and μ_{ref} is the reference viscosity at a reference temperature and was taken as $1.002 \text{ kg}/(\text{m}\cdot\text{s})$ ¹⁵.

The temperature dependence of water density and water viscosity can be given as:

$$\rho = 1152.3 - 0.5116 \times T_k \quad (43)$$

$$\mu = \mu_{ref} \times 10^{\frac{1.3272(20-T_c)-0.001053(20-T_c)^2}{T_c+105}} \quad (44)$$

where T_C , T_K is temperature in $^\circ\text{C}$ and Kelvin respectively.

Since water molecules are readily available at the metal surface, it can be assumed that at all times the reduction rate of H_2O is controlled by the charge-transfer process, and hence, the Tafel equation is used:

$$i_{H_2O} = i_{0,H_2O} \times 10^{\frac{\eta}{b_c}} \quad (45)$$

Tafel slope for this reaction in all experiments at 30°C was found to be close to 120 mV/decade, which is the same as that for H^+ reduction. Tafel slope for H_2O reduction is given by Equation (36).

Since the electrochemical reduction of H_2O and H^+ are equivalent thermodynamically, the reversible potential of H_2O reduction were assumed to be the same as for H^+ reduction, which is calculated by Equation (37).

The exchange current density for H_2O reduction is given by:

$$i_{0,\text{H}_2\text{O}} = i_0^{\text{ref}} \left(\frac{c_{\text{H}^+}}{c_{\text{H}^+ \text{ ref}}} \right)^{-0.5} e^{-\frac{\Delta H}{R} \left(\frac{1}{T} - \frac{1}{T_{\text{ref}}} \right)} \quad (46)$$

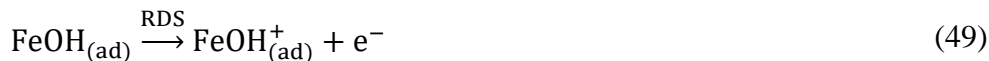
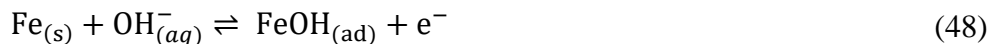
The $i_{0,\text{ref}}$ for H_2O reduction was taken as $2 \times 10^{-5} \text{ A/m}^2$ at reference temperature 293.15K and reference H^+ concentration $1 \times 10^{-4} \text{ mol/L}$. The enthalpy of activation was taken as 30 kJ/mol¹¹.

3.1.2 Anodic Reaction

Iron dissolution is an oxidation reaction following:



Since this is actually a multistep reaction, Bockris *et al.*¹⁰ proposed the following mechanism of anodic iron dissolution in strong acids ($\text{pH} \leq 4$):



This mechanism suggests that the reaction order with respect to OH^- ions is 1, which is proven to be valid in more acidic solutions; it has also been found that iron dissolution proceeds with little influence of pH for solutions where pH is approximately pH 4 or above ¹⁰.

It is assumed that the anodic dissolution of iron is under charge transfer control. Thus, pure Tafel behavior can be assumed close to the corrosion potential:

$$i_{Fe} = i_{0,Fe} \times 10^{\frac{\eta}{b_a}} \quad (51)$$

The Tafel slopes of anodic reaction are in the range of 40-50 mV/decade. For anodic iron dissolution the Tafel slope is given as:

$$b_a = \frac{2.303RT}{\alpha_a F} \quad (52)$$

According to Bockris, *et al.*,¹⁰ the apparent symmetry coefficient for the anodic reaction of Fe dissolution was taken as 1.5, giving $b_a = 40$ mV at 30°C. The reversible potential of X-65 steel was taken^{1, 11} to be – 0.488 V.

According to the mechanism proposed by Bockris *et al.*,¹⁰ the reaction order with respect to OH⁻ ions is 1, which is truly valid only in more acidic solutions. When the solution pH is above approximately 4, it has been found that iron dissolution proceeds with little influence of pH. It is assumed that the exchange current density is proportional to the surface coverage of OH⁻ (θ_{OH^-}) and it follows the Frumkin adsorption model:

$$i_{0,Fe} = i_{0,Fe}^* \theta_{OH^-} e^{-\frac{\Delta H}{R} \left(\frac{1}{T} - \frac{1}{T_{ref}} \right)} \quad (53)$$

$$K_1 c_{OH^-} = \frac{\theta_{OH^-}}{1 - \theta_{OH^-}} e^{(-f\theta_{OH^-})} \quad (54)$$

According to the current experimental results and Bockris *et al.*¹⁰, the best-fit values in Equation (53) and (54) are $i_{0,Fe}^* = 0.25$, $K_1 = 1.56 \times 10^9$ and $f = 3.83$. Actually when f is equal to 0, the Frumkin adsorption model becomes the Langmuir adsorption

model. The reference temperature is 293.15K. The activation energy ΔH was set to be 37.5 kJ/mol, which is taken from the finding of Nešić *et al.*¹¹.

The concentration of OH^- can be calculated by the water chemistry model in Chapter 2.

3.1.3 *The Mixed Potential Theory*

The corrosion potential then can be calculated by solving the charge balance equation at the metal surface:

$$\sum i_a = \sum i_c \quad (55)$$

which here takes the form:

$$i_{\text{Fe}} = i_{\text{H}^+} + i_{\text{H}_2\text{O}} \quad (56)$$

Once the corrosion potential is found, the corrosion current and rate can be found from the anodic current (or the sum of cathodic current) at the corrosion potential.

The individual and total cathodic and anodic currents can also be calculated at any given potential, and full curves of the predicted potentiodynamic sweeps can be then readily generated, as done in the steady state model of FREECORP™ 2.0 (similar to how it was done in FREECORP 1.0).

3.1.4 *Model Verification*

Performance of the model was validated by comparing the predictions with the experimental data and the results are presented in Figure 9 and Figure 10.

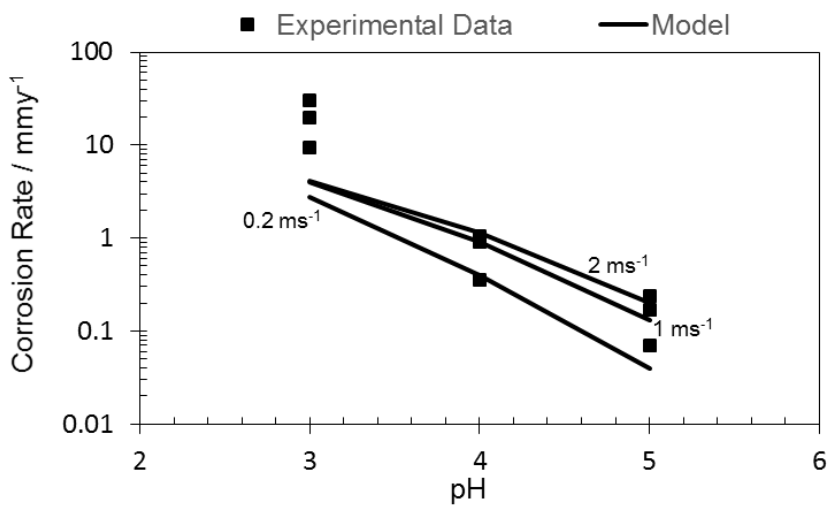


Figure 9. Comparison of predicted corrosion rate with LPR experimental results at different speed and pH values, total pressure=1.0 bar, 20°C, points: experimental results, solid lines: predicted curves, $B = 23 \text{ mV/ decade}$.

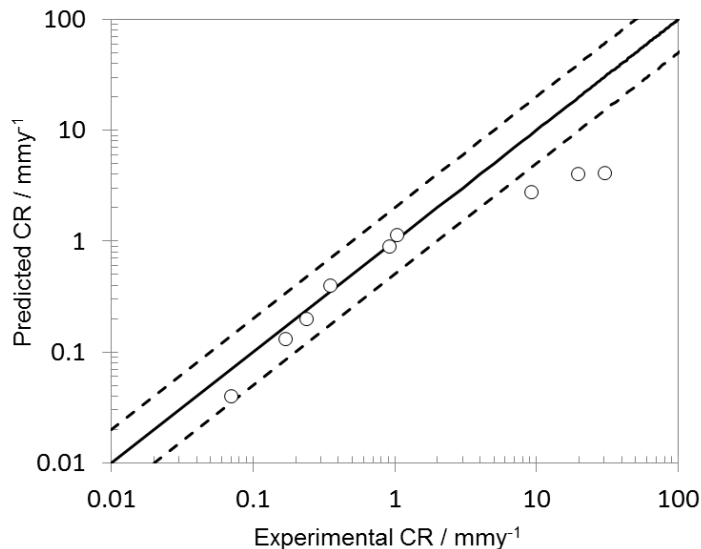


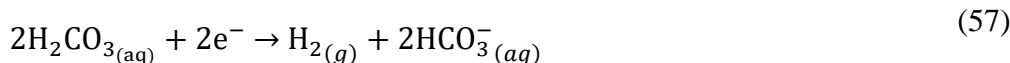
Figure 10. Parity plot showing a direct comparison of predicted and experimental corrosion rates; total pressure 1 bar, pH 3.0 to 5.0, $v = 0.2, 1, \text{ and } 2 \text{ m/s}$. The solid line represents perfect agreement of experimental and calculated corrosion rates. The dashed lines represent a factor of 2 deviation.

3.2 Aqueous CO₂ Environment

3.2.1 Cathodic Reaction

There are three cathodic reactions in a CO₂ aqueous system. The details of H⁺ reduction and H₂O reduction have been described in 2.4, and no change is made for a CO₂ aqueous system. However, modeling of H₂CO₃ reduction is an additional reaction and will be addressed below.

Direct H₂CO₃ reduction is represented by:



Modeling of H₂CO₃ reduction for a pure CO₂ aqueous system has been clearly described clearly by Nešić *et al.*¹ The total current density of H₂CO₃ reduction is given by:

$$\frac{1}{i_{\text{H}_2\text{CO}_3}} = \frac{1}{i_{\alpha,\text{H}_2\text{CO}_3}} + \frac{1}{i'_{\text{lim},\text{H}_2\text{CO}_3}} \quad (58)$$

where $i_{\text{H}_2\text{CO}_3}$, $i_{\alpha,\text{H}_2\text{CO}_3}$ and $i'_{\text{lim},\text{H}_2\text{CO}_3}$ are the total current density, the charge transfer current density and the mass transfer limiting current density of this reaction in A/m², respectively.

Charge transfer current density of this reaction can be calculated using the equation:

$$i_{\alpha,\text{H}_2\text{CO}_3} = i_{0,\text{H}_2\text{CO}_3} \times 10^{-\frac{\eta}{b_c}} \quad (59)$$

Tafel slope and reversible potential can be calculated from Equations (60) and Equations (61)

$$b_c = \frac{2.303RT}{\alpha_c F} \quad (60)$$

$$E_{rev} = -\frac{2.303RT}{F} pH - \frac{2.303RT}{2F} \log p_{H_2} \quad (61)$$

where $\alpha_c = 0.5$ giving $b_c \approx 0.120$ V/decade at 30°C, and the p_{H_2} is set to 1 bar.

The exchange current density can be calculated by:

$$i_{0,H_2CO_3}^r = i_0^{ref} \left(\frac{c_{H_2CO_3}}{c_{H_2CO_3\ ref}} \right)^{0.5} \left(\frac{c_{H^+}}{c_{H^+\ ref}} \right)^{-0.5} \times e^{\frac{\Delta H}{R} \left(\frac{1}{T} - \frac{1}{T_{ref}} \right)} \quad (62)$$

the i_{0ref} for H_2CO_3 reduction was taken to be 0.014 A/m² at 293.15K reference temperature and 1×10^{-4} mol/L reference H_2CO_3 concentration. The enthalpy of activation in Equation (62) is set to 50 kJ/mol.

The CO_2 hydration reaction limiting current density can be calculated using ¹⁶:

$$i_{lim(H_2CO_3)}^r = f \times F c_{CO_2} \times (D_{H_2CO_3} K_{hyd} k_{hyd}^f)^{0.5} \quad (63)$$

where c_{CO_2} is the bulk concentration of dissolved carbon dioxide, which can be obtained from the water chemistry model in Chapter 2. k_{hyd}^f is the forward hydration reaction constant, which is given as ⁵ :

$$k_{hyd}^f = 10^{\frac{329.85 - 110.541 \times \log T_k - \frac{17265.4}{T_k}}{}} \quad (64)$$

3.2.2 Anodic Reaction

The only anodic reaction is iron dissolution from the steel surface, as reaction (65) shows. This reaction is already described in 2.4 for strong acid solution and will be modified for a pure CO_2 environment.



The detailed model of iron dissolution in a CO₂ environment has been reported by Nesic *et al.*¹ This reaction is under charge transfer control. Thus, pure Tafel behavior can be assumed close to the corrosion potential.

$$i_{Fe} = i_{0,Fe} \times 10^{\frac{\eta}{b_a}} \quad (66)$$

The reference exchange current density $i_{0,Fe}^*$ at room temperature, 293.15K is 1 A/m² for X-65 steel. The activation energy ΔH was found to be 37.5 kJ/mol. The Tafel slope is $b_a = \frac{2.303RT}{1.5F}$. The reversible potential of X-65 steel was taken to be – 0.488 V^{1,11}.

3.2.3 The Mixed Potential Theory

The corrosion potential then can be calculated by solving the charge balance equation:

$$\sum i_a = \sum i_c \quad (67)$$

which here takes the form:

$$i_{Fe} = i_{H_2CO_3} + i_{H^+} + i_{H_2O} \quad (68)$$

Once the corrosion potential is known, the corrosion current and rate can be found from the anodic current (or the sum of cathodic current) at the corrosion potential. The individual and total cathodic and anodic curves, and predicted potentiodynamic sweeps can be then readily generated, as done in the steady state model of FREECOPR™ 2.0 (similar to how it was done in FREECOPR 1.0).

3.2.4 Model Verification

The electrochemical model in a pure CO₂ environment is validated with the experimental results at pH 4.0 and pH 5.0. Figure 11 and Figure 12 show the comparison of the potentiodynamic sweeps simulated by the model with experimental data. It can be seen that the potentiodynamic sweeps capture the corrosion processes very well, and the calculated results are in a very good agreement with all experimental results.

Figure 13 and Figure 14 shows a good agreement between the experimental results and the calculated values from the model.

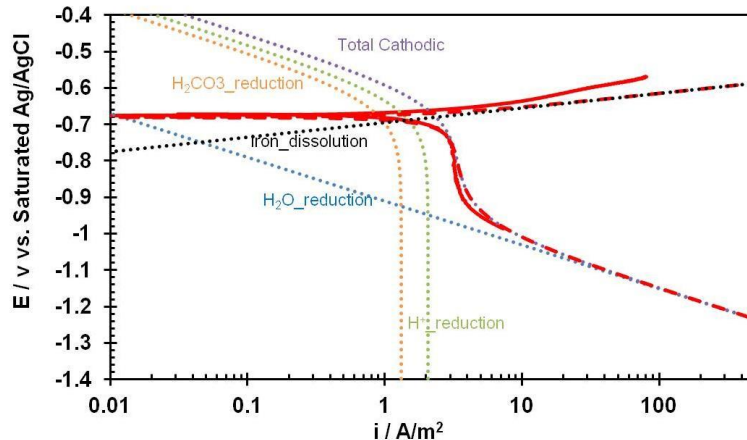


Figure 11. Comparison between predicted potentiodynamic sweeps and experimental results in the solution purged with pure CO₂ at pH 4.0, 30°C, total pressure of 1 bar, 1 wt% NaCl, 1000rpm rotating speed, exposure time < 2 hours.

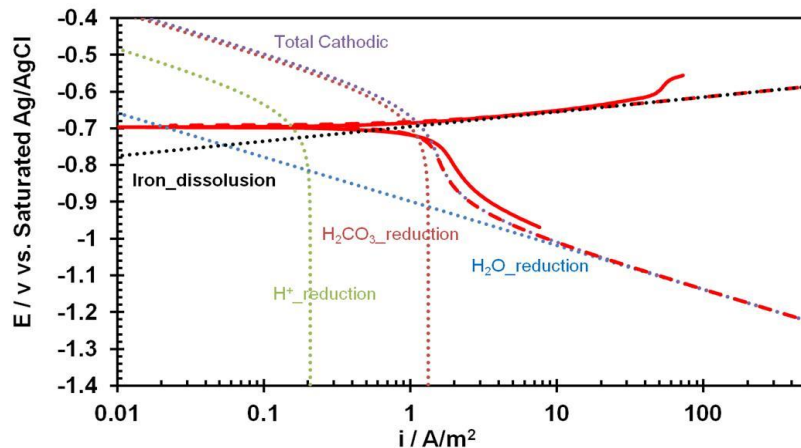


Figure 12. Comparison between predicted potentiodynamic sweeps and experimental results in the solution purged with pure CO₂ at pH 5.0, 30°C, total pressure of 1 bar, 1 wt% NaCl, 1000rpm rotating speed, exposure time < 2 hours. Dashed line is for prediction and solid line is for experimental.

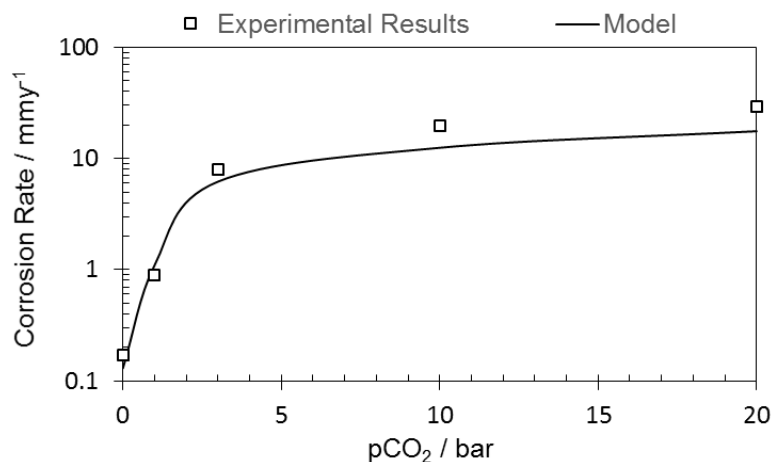


Figure 13. Comparison of predicted corrosion rate with LPR experimental results at different speed, pH 5.0, 60°C, points: experimental results, solid lines: predicted curves, B = 23 mV/ decade.

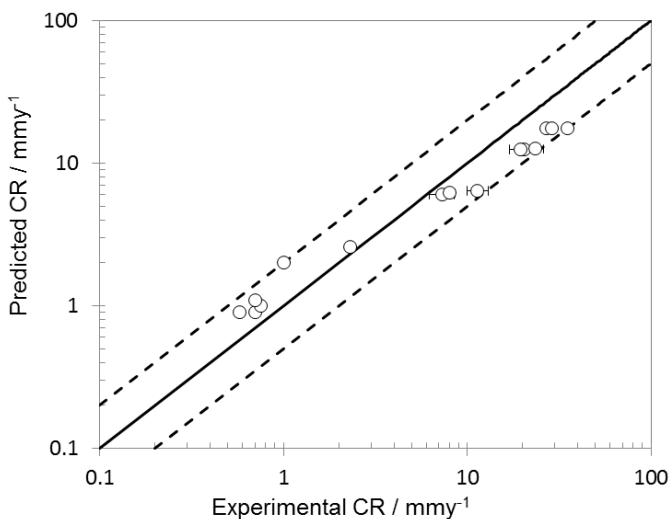
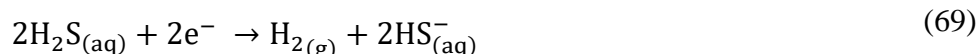


Figure 14. Parity plot showing a direct comparison of predicted and experimental corrosion rates; total pressure 1 bar, pH 3.0 to 5.0, $v = 0.2, 1, \text{ and } 2 \text{ m/s}$. The solid line represents perfect agreement of experimental and calculated corrosion rates. The dashed lines represent a factor of 2 deviation.

3.3 Aqueous H₂S Environment

3.3.1 Cathodic Reactions

It has been experimentally proven that H₂S adsorbed on the steel surface can also be an electron acceptor ¹⁷ and the evolution of hydrogen can occur via the so called direct reduction of H₂S:



This reaction has a limiting current which is controlled by a mass transfer rate of H₂S from bulk solution to the steel surface, and is therefore sensitive to flow.

The total current density for direct reduction of H₂S is given by:

$$\frac{1}{i_{H_2S}} = \frac{1}{i_{\alpha,H_2S}} + \frac{1}{i_{\lim,H_2S}^d} \quad (70)$$

where i_{H_2S} , i_{α,H_2S} and i_{\lim,H_2S}^d are total current density, charge transfer current density and mass transfer limiting current density of H_2S reduction in A/m^2 , respectively.

Charge transfer current density of H_2S reduction can be calculated using the equation:

$$i_{\alpha,H_2S} = i_{0,H_2S} \times 10^{-\frac{\eta}{b_c}} \quad (71)$$

where i_{0,H_2S} represents the exchange current density in A/m^2 , b_c represents the cathodic Tafel slope in V/decade for H_2S reduction, and η represents the over potential in V, which is equal to the difference between the operating (actual) potential and the reversible potential.

From the experiments, the cathodic Tafel slope b_c for H_2S reduction in Equation (71) was found to be close to 120 mV/decade at 30°C, which is the same as the value used for H^+ reduction. The value of b_c can be calculated from Equation (36).

From the best fit to experimental results at different concentration of H_2S at pH 4, the order n of the reaction with respect to C_{H_2S} is found to be:

$$\frac{\partial \log i_{0,H_2S}}{\partial \log C_{H_2S}} \approx 0.5 \quad (72)$$

The same reaction order of 0.5 was also suggested by J. Kittel *et al.*¹⁸. It is similar to the one associated with the exchange current density of H^+ reduction. Morris *et al.*¹⁹ and Cheng *et al.*²⁰ stated that corrosion reaction order with H_2S : $n = \partial(\log i_{corr}/\partial \log C_{H_2S}) = 0.2$. However, i_{corr} includes both contributions from H^+ and H_2S reduction. Under their

experimental conditions (pH from 0.75 to 4), the contribution from H^+ is dominant and would not allow an accurate calculation of the H_2S reduction reaction order.

Therefore, the exchange current density can be calculated as:

$$i_{0,\text{H}_2\text{S}} = i_{0,\text{H}_2\text{S}}^{\text{ref}} \left(\frac{c_{\text{H}_2\text{S}}}{c_{\text{H}_2\text{S}}^{\text{ref}}} \right)^{0.5} \times \left(\frac{c_{\text{H}^+}}{c_{\text{H}^+}^{\text{ref}}} \right)^{-0.5} \times e^{-\frac{\Delta H_{\text{H}_2\text{S}}}{R} \left(\frac{1}{T} - \frac{1}{T_{\text{ref}}} \right)} \quad (73)$$

where the i_0^{ref} for H_2S reduction is taken as 0.0006 A/m^2 at a reference temperature of 293.15K and a reference H^+ concentration of $1 \times 10^{-4} \text{ mol/L}$, and a reference H_2S concentration of $1 \times 10^{-4} \text{ mol/L}$. This means that the H_2S reduction rate is about 50 times slower than the H^+ reduction rate (0.03 A/m^2) at the same condition. The enthalpy of activation was taken as 60 kJ/mol from the best fit to experimental results.

The two electrochemical reactions, the reductions of H_2S and H^+ , are equivalent thermodynamically and have the same reversible potential given by Equation (61). Calculation of limiting current density for H_2S reduction is similar to that for H^+ reduction. The mass transfer limiting current density of this reaction is given by:

$$i_{\text{lim},\text{H}_2\text{S}}^d = k_{m,\text{H}_2\text{S}} F c_{\text{H}_2\text{S}} \quad (74)$$

$$Sh = 0.0165 \times Re^{0.86} \times Sc^{0.33} \quad (75)$$

$$D_{\text{H}_2\text{S}} = D_{\text{ref}(\text{H}_2\text{S})} \times \frac{T_k}{T_{\text{ref}}} \times \frac{\mu_{\text{ref}}}{\mu} \quad (76)$$

where $D_{\text{ref}(\text{H}_2\text{S})}$ was taken as $1.61 \times 10^{-9} \text{ m}^2/\text{s}$ at reference temperature (293.15 K)²¹

The concentration of H_2S can be calculated from the water chemistry model in section Chapter 2.

When H₂S is present, it can retard the H₂O reduction, resulting in rates about 20 times lower than that seen in environments without H₂S, suggesting competitive adsorption at the steel surface. From the current experimental results, the reaction order log $i_{0,H_2O}/\log_{CH_2S}$ is close to 0.1. The exchange current density is given by:

$$i_{0,H_2O} = i_{0,H_2O}^{ref} \left(\frac{c_{H_2S}}{c_{H_2S}^{ref}} \right)^{-0.2} \times \left(\frac{c_{H^+}}{c_{H^+}^{ref}} \right)^{-0.5} \times e^{-\frac{\Delta H}{R} \left(\frac{1}{T} - \frac{1}{T_{ref}} \right)} \quad (77)$$

In an H₂S environment, the i_0^{ref} for H₂O reduction was taken as 1×10^{-6} A/m² at reference temperature 293.15K, the reference H⁺ concentration of 1×10^{-4} mol/L, and the reference H₂S concentration of 1×10^{-4} mol/L. The enthalpy of activation was taken as 90 kJ/mol from the best fit to experimental results, which would suggest that H₂O reduction in an H₂S environment is more sensitive to temperature.

3.3.2 Anodic Reaction

In a solution containing H₂S, the anodic reaction rate is related to HS⁻ ions adsorption. The mechanism is similar to the one proposed by Bockris *et al.*¹⁰ and is shown²²:



The Tafel slopes of anodic reaction in a H₂S environment is similar to the Tafel slop in environments without H₂S, a value in the range of 40-50 mV/decade. The

introduction of H₂S did not have any effect on the Tafel slope, so for anodic iron dissolution the Tafel slope is given as:

$$b_a = \frac{2.303RT}{\alpha_a F} \quad (82)$$

When H₂S is present, according to the mechanism proposed previously, Equations (78) to (81), the exchange current density for iron dissolution is related to HS⁻ concentration. Even at low concentrations of H₂S, such as 100 ppm (v) H₂S (0.1 mbar) and pH 4, the concentration of HS⁻ is much higher (1×10^{-8} mol/L) than the concentration of OH⁻ (1×10^{-10} mol/L). Therefore, the contribution of OH⁻ to the anodic reaction kinetics was ignored. It can be assumed that the exchange current density is only related to the surface coverage of HS⁻ (θ_{HS^-}) and that it follows the Langmuir adsorption model:

$$i_{0,Fe} = i_{0,Fe}^{*} \theta_{HS^-} e^{-\frac{\Delta H}{R} \left(\frac{1}{T} - \frac{1}{T_{ref}} \right)} \quad (83)$$

$$\theta_{HS^-} = \frac{K_2 c_{HS^-}}{1 + K_2 c_{HS^-}} \quad (84)$$

The best fit values for $i_{0,Fe}^{*}$ and K_2 in Equation (83) and (84) are $i_{0,Fe}^{*} = 0.25$, $K_2 = 3.5 \times 10^6$. The reference temperature is 293.15 K. The activation energy ΔH was assumed to be the same as that for an environment without H₂S (37.5 kJ/mol). c_{HS^-} is the concentration of HS⁻, which is given by the water chemistry model in Chapter 2.

3.3.3 The Mixed Potential Theory

The corrosion potential then can be calculated by solving the charge balance equation:

$$\sum i_a = \sum i_c \quad (85)$$

which here takes the form:

$$i_{Fe} = i_{H_2S} + i_{H^+} + i_{H_2O} \quad (86)$$

Once the corrosion potential is known, the corrosion current and rate can be found from the anodic current (or the sum of cathodic current) at the corrosion potential. The individual and total cathodic and anodic curves, and predicted potentiodynamic sweeps can be then readily generated, as done in the steady state model of FREECORP™ 2.0 (similar to how it was done in FREECORP 1.0).

3.3.4 Model Verification

Performance of the model was validated by comparing the predictions with experimental results. Even if some of the same empirical data are used for this comparison which formed a basis for calibrating the constants in the model, the complexity of the physicochemical phenomena present a real challenge for the mechanistic model. Good agreement across the different conditions can be expected only if the fundamental assumptions underlying the model are correct, and of course, if the calibration was done properly. Further testing with the model using external data was done and described in the following sections.

3.3.4.1 Effect of pH_2S

Figure 15 shows that the predicted corrosion rates from the electrochemical model are in good agreement with experimental results, which suggests that the electrochemical model captured the main effects of H_2S corrosion of mild steel in the absence of iron sulfide.

Figure 16, Figure 17, Figure 18 show cathodic and anodic polarization curves changing with H_2S concentration for the different pH aqueous environments. The model prediction successfully captures the anodic reaction change in the low pH range (Figure 17, for pH 3.0) and the cathodic reaction change in high pH environments (Figure 18, for pH 5.0) due to the additional cathodic reaction: H_2S reduction. Predicted potentiodynamic sweeps are in good agreement with experimental results for individual reactions generated with the present model.

Using this kind of model, the cathodic polarization curves can be deconvoluted to show the contribution from three individual cathodic reactions (H^+ reduction, H_2S reduction and H_2O reduction). It can be seen, for example, that when increasing the H_2S concentration, the H^+ reduction doesn't change; that the H_2S reduction curve moves to the higher values of the current (on the right of the graph), and that H_2O reduction changes only a little; see Figure 16, Figure 17, and Figure 18.

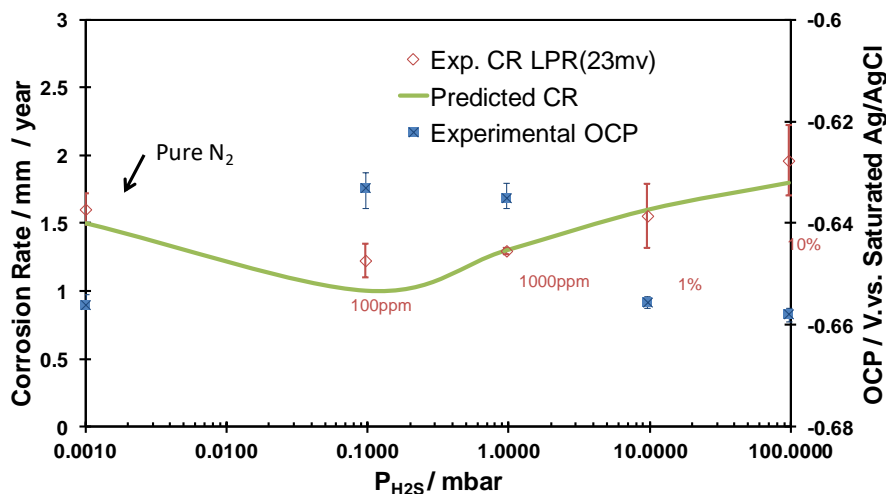


Figure 15. Comparison of corrosion rate predictions with LPR experimental results and experimental OCP at pH 4.0 and different H_2S concentration, total pressure=1.0 bar, 1000rpm 30°C, B = 23 mV/ decade. Here the error bars represent standard

deviation of mean value, which calculated from the multiple LPR measurements. The error bars in the following text were obtained with the same method.

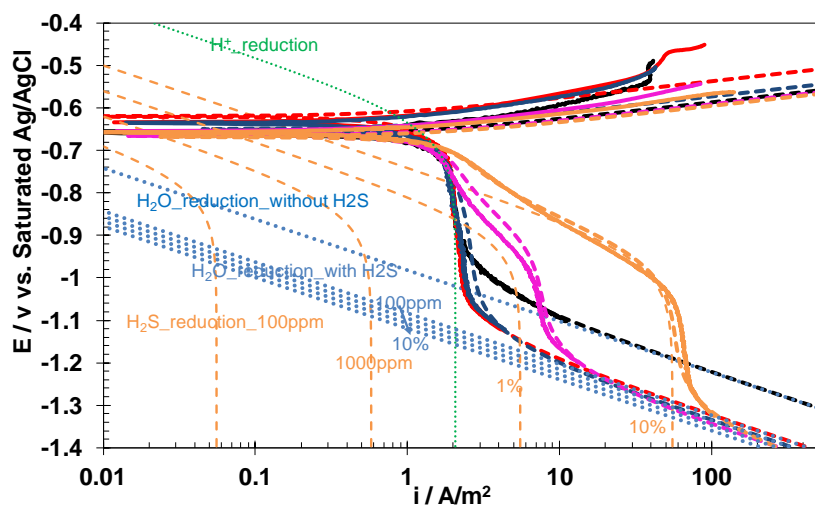


Figure 16. Comparison of predicted polarization curves with experimental results at different H_2S concentration, pH 4.0, total pressure=1.0 bar, 1000rpm, 30°C. Solid line: experimental curves. Dashed line: predicted curves. Black: 0 ppm(v) $\text{H}_2\text{S(g)}$, Red: 100 ppm(v) $\text{H}_2\text{S(g)}$, Dark blue: 1000 ppm(v) $\text{H}_2\text{S(g)}$, Pink: 1%(v) $\text{H}_2\text{S(g)}$, purple: 10%(v) $\text{H}_2\text{S(g)}$.

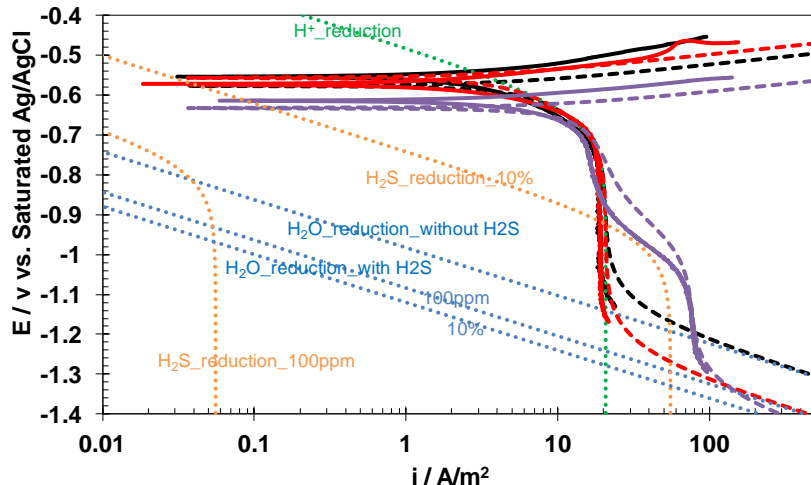


Figure 17. Comparison of predicted polarization curves sweeps with experimental results at different H_2S concentration, pH 3.0, total pressure=1.0 bar, 1000rpm, 30°C. Solid line: experimental curves. Dashed line: predicted curves. Black: 0 ppm(v) $\text{H}_2\text{S(g)}$, red: 100 ppm(v) $\text{H}_2\text{S(g)}$, purple: 10%(v) $\text{H}_2\text{S(g)}$.

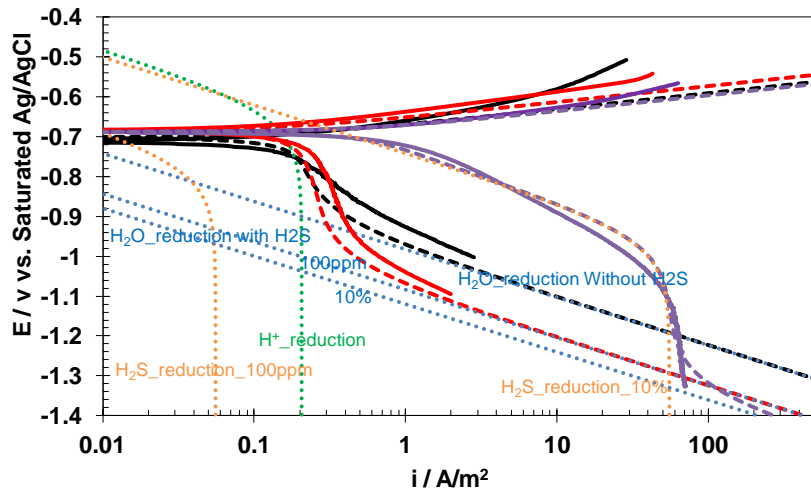


Figure 18. Comparison of predicted polarization curves with experimental results at different H_2S concentration, pH 5.0, total pressure=1.0 bar, 1000rpm, 30°C. Solid line: experimental curves. Dashed line: predicted curves. Black: 0 ppm(v) $\text{H}_2\text{S(g)}$, red: 100 ppm(v) $\text{H}_2\text{S(g)}$, purple: 10%(v) $\text{H}_2\text{S(g)}$.

3.3.4.2 Effect of Flow Rate

The effect of flow rate on both cathodic reaction and anodic reaction at 1%(v) and 10%(v) H₂S(g) is depicted in Figure 20 and Figure 21. Increasing flow (rotating speed) does not affect the anodic reaction and H₂O reduction which are both under charge transfer control, but accelerates the cathodic reaction due to the increase of mass transfer rate related to H⁺ reduction and H₂S reduction. Except for the case of the limiting current density at 200 rpm rotating speed, all the predicted polarization curves agree well with the experimental results. Corrosion rate predictions are shown in Figure 19. The predicted corrosion rates are close to the experimental results.

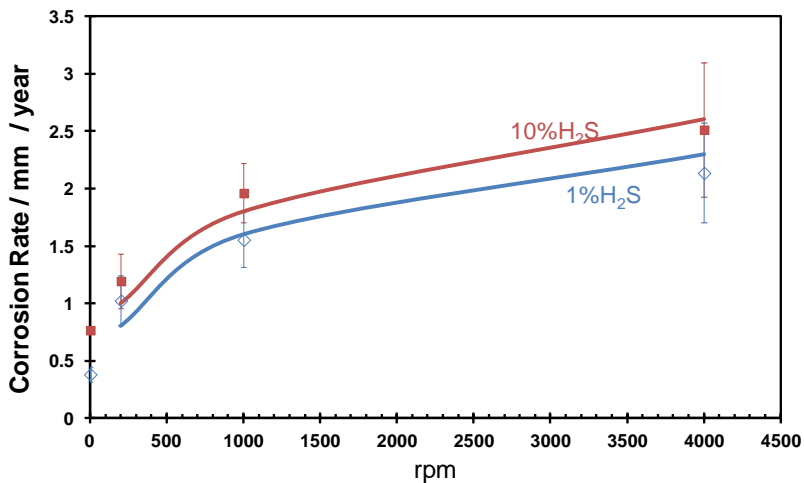


Figure 19. Comparison of predicted corrosion rate with LPR experimental results at different rotational speed, pH 4.0, total pressure=1.0 bar, 30°C, points: experimental results, solid lines: predicted curves, B = 23 mV/ decade.

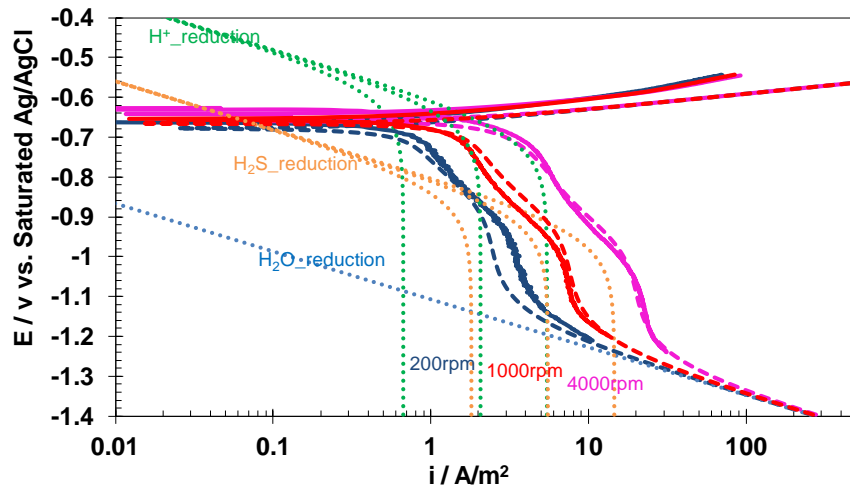


Figure 20. Comparison of predicted polarization curves with experimental results at different rotated speed, pH 4.0, 1%(v) $\text{H}_2\text{S(g)}$, total pressure=1.0 bar, 30°C. Solid line: experimental curves. Dashed line: predicted curves. Dark: 200rpm, red: 1000rpm, pink: 4000rpm.

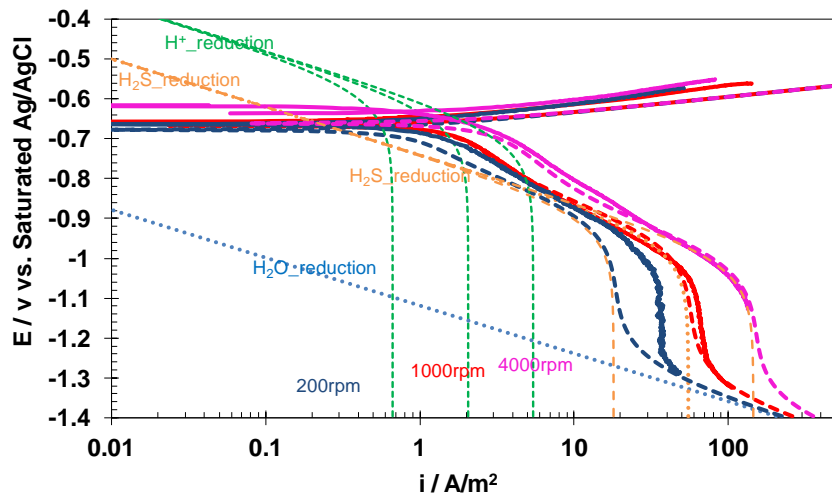


Figure 21. Comparison of predicted polarization curves with experimental results at different rotated speed, pH 4.0, 10%(v) $\text{H}_2\text{S(g)}$, total pressure=1.0 bar, 30°C. Solid line: experimental curves. Dashed line: predicted curves. Dark blue: 200rpm, red: 1000rpm, pink: 4000rpm.

3.3.4.3 Effect of pH

Comparison between predicted polarization curves and experimental polarization curves in solution without H₂S are shown in Figure 22. A good agreement is found at each pH. From Figure 22, H⁺ reduction curves shift to the higher current values on the right with pH decreasing while anodic reaction curves move to lower values on the left with pH decreasing.

When 100 ppm(v) H₂S(g) is present, the prediction of polarization curves is shown in Figure 23. Due to the low concentration of H₂S in solution, no obvious effect on the cathodic polarization curve is observed. As mentioned previously, the anodic reaction is related to the HS⁻ concentration. At the same gas concentration of H₂S, c_{Ac^-} is inversely proportional to the pH, so the anodic reaction rate increases with pH increase. The experimental and predicted polarization curves were found to be in very good agreement.

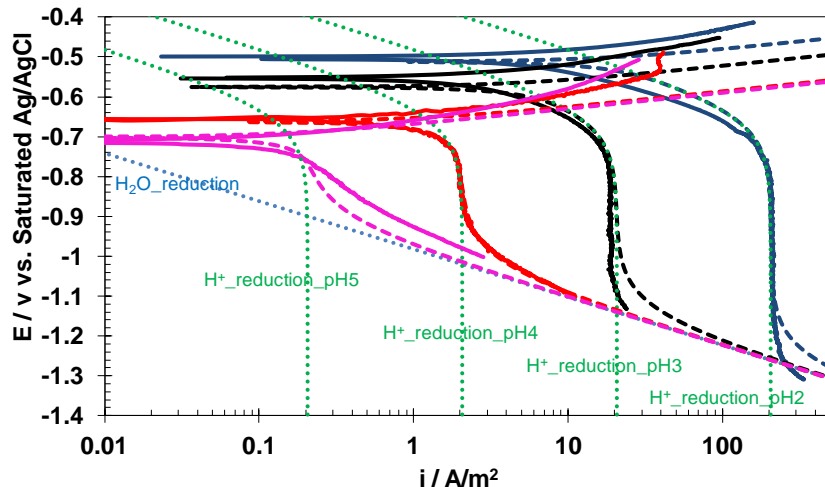


Figure 22. Comparison of predicted polarization curves with experimental results at different pH, 1000rpm, 0 ppm(v) H₂S (g), total pressure=1.0 bar, 30°C. Solid line:

experimental curves. Dashed line: predicted curves. Pink: pH 5.0, Dark blue: pH 2.0, black: pH 3.0, red: pH 4.0, pink: pH 5.0.

For 10% (v) $\text{H}_2\text{S(g)}$ present, the comparison of the predicted polarization curves with the experimental results is shown in Figure 24. It is evident that the predicted polarization curve at each pH is in good agreement with the experimental result. When the H_2S concentration is higher the H_2S reduction affects the overall cathodic polarization curves significantly. Anodic polarization curves are not sensitive to pH in Figure 24 due to the high concentration of HS^- .

Corrosion rate prediction at a different pH is shown in Figure 25. The electrochemical model predictions are in good agreement with experimental results, which means the electrochemical model captured the main features of H_2S corrosion at a different pH.

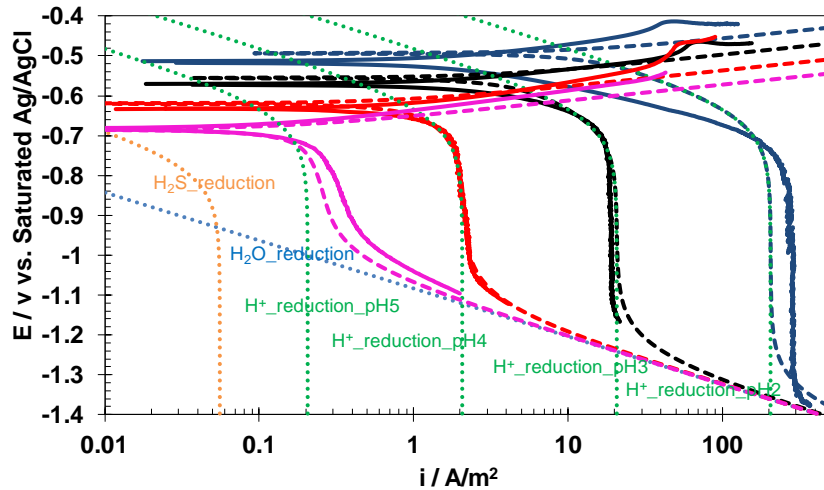


Figure 23. Comparison of predicted polarization curves with experimental results at different pH, 1000rpm, 100 ppm(v) $\text{H}_2\text{S(g)}$, total pressure=1.0 bar, 30°C. Solid line: experimental curves. Dashed line: predicted curves. Pink: pH 5.0, Dark blue: pH 2.0, black: pH 3.0, red: pH 4.0, pink: pH 5.0.

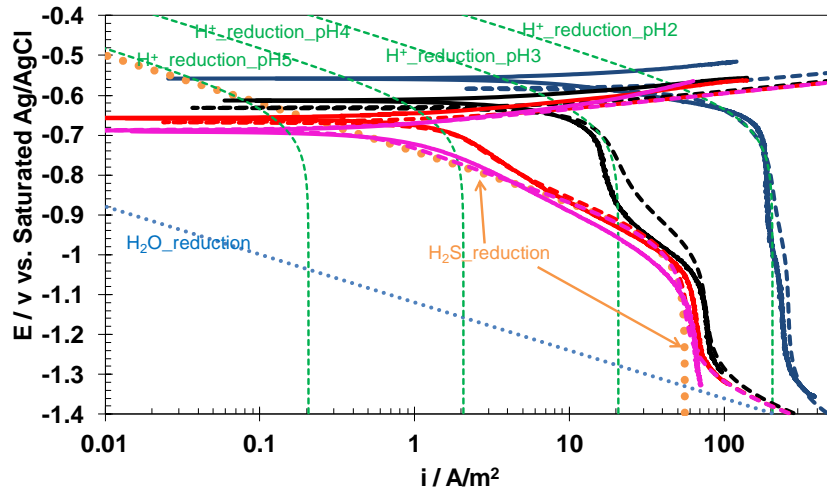


Figure 24. Comparison of predicted polarization curves with experimental results at different pH, 1000rpm, 10%(v) $\text{H}_2\text{S(g)}$, total pressure=1.0 bar, 30°C. Solid line: experimental curves. Dashed line: predicted curves. Dark blue: pH 2.0, black: pH 3.0, red: pH 4.0, pink: pH 5.0.

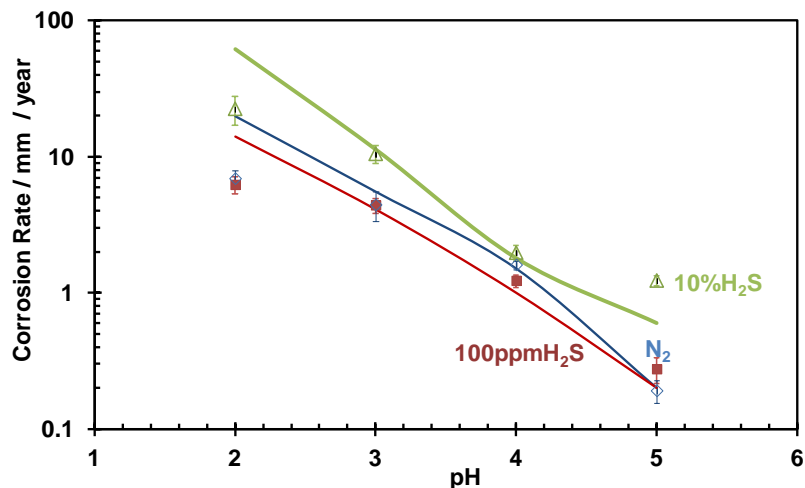


Figure 25. Comparison of predicted corrosion rate with experimental results at different pH, different H_2S concentration, 1000rpm, and total pressure=1.0 bar, 30°C, point: experimental results, solid line: predicted curves. LPR constant B = 23 mV/ decade.

3.3.4.4 Effect of Temperature

The effect of temperature on both cathodic reaction and anodic reaction at $c_{\text{H}_2\text{S}} = 8.3 \times 10^{-4} \text{ M}$ is depicted in Figure 26. Increasing temperature has a small influence on the

anodic reaction, but accelerates the cathodic reaction greatly. H^+ reduction, H_2S reduction and H_2O reduction rate increase with temperature increase. All the predicted sweeps agree with experimental results well.

Corrosion rate predictions are shown in Figure 27. This electrochemical model captures well the corrosion rate change with temperature.

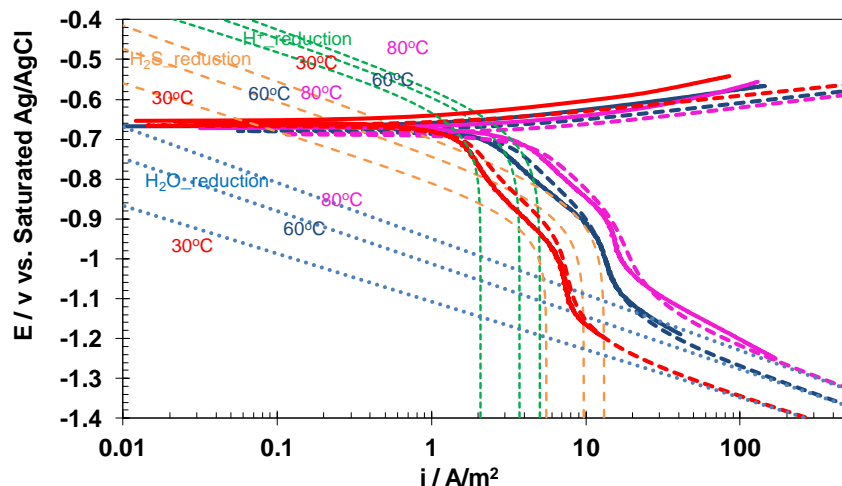


Figure 26. Comparison of predicted polarization curves with experimental results at different temperature, 1000rpm, $c_{\text{H}_2\text{S}} = 8.3 \times 10^{-4} \text{ mol/L}$, total pressure=1.0 bar, 30°C. Solid line: experimental curves. Dashed line: predicted curves. Red: 30°C, Dark blue: 60°C, pink: 80°C.

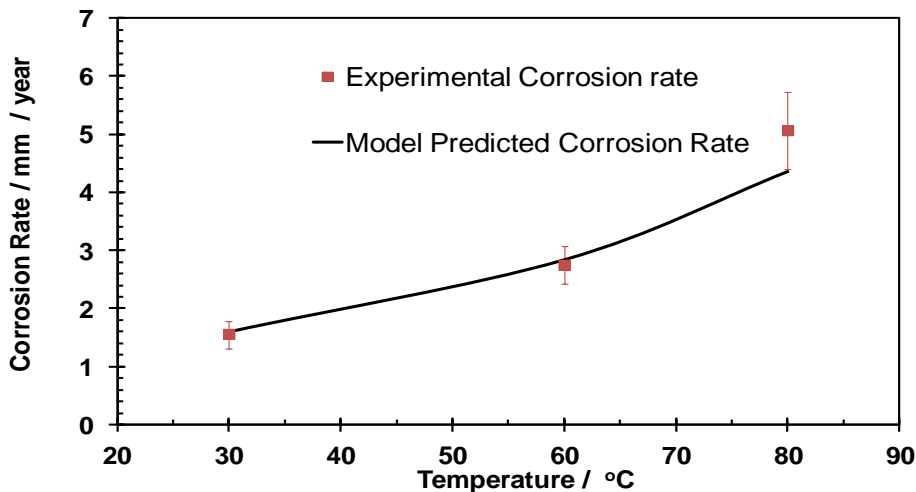


Figure 27. Comparison of predicted corrosion rate with experimental results at different temperature, 1000rpm, $c_{H_2S} = 8.3 \times 10^{-4}$ mol/L, total pressure=1.0 bar, 30°C, Point: experimental results, solid line: predicted curves. LPR constant B = 23 mV/ decade.

3.3.4.5 Higher H_2S partial pressures

In Figure 27 (a) the measured data points show an average obtained from five repeats, conducted at the pH 3.0. There is a very good agreement between the measured data and the calculated ones, particularly at the lower current densities (< 10 A/m²). The deviation in the limiting current at very high current densities (> 500 A/m²) was probably due to excessive formation of hydrogen gas bubbles at the electrode surface. The existence of the so called “double wave” comes from the two independent cathodic reactions and their limiting currents.²³⁻²⁴

Similar results were obtained at pH 4.0, see Figure 27 (b), which shows the averages of the data collected from four repeated experiments. Data from the experiments conducted at pH 5.0 are presented in Figure 27 (c), which shows the averages from experiments repeated six times. It is clear that at the higher pH values, the reduction of

H_2S dominates the rate of the cathodic reaction, as a result of a lower rate of H^+ reduction due to a lower concentration of H^+ ions. There seems to be a slight deviation between the measured and calculated Tafel slope for H_2S reduction, which is difficult to explain. It may be due to a measurements error obtained at the higher current densities ($>10 \text{ A/m}^2$) or a result of the inaccuracy of the model at these conditions. Either way, this is not expected to affect the corrosion rate calculation in a significant way, since the corrosion current densities are typically below 10 A/m^2 .

For data collected at pH 5.0, presented in Figure 27 (c), there is an approximately 50 mV deviation between the calculated and the measured OCP. This problem is most likely associated with the modeling of the anodic (iron dissolution) current. To confirm this and eliminate any possible experimental error associated with iron sulfide layer formation during the cathodic sweeps (which were conducted first), a new experiment was organized where the anodic sweep was conducted on a freshly polished specimen. The results were consistent and provided conclusive evidence that the OCP deviation was not a result of erroneous measurements. It is difficult to postulate what the exact problem is, without a more extensive investigation of the anodic reaction in H_2S environments, which exceeds the scope of the present paper. It is worth noting that the effect of adsorbed OH^- on the rate of anodic iron dissolution was not considered in the model²³. However, whether this is the main cause of the discrepancy seen at pH 5.0 requires further research.

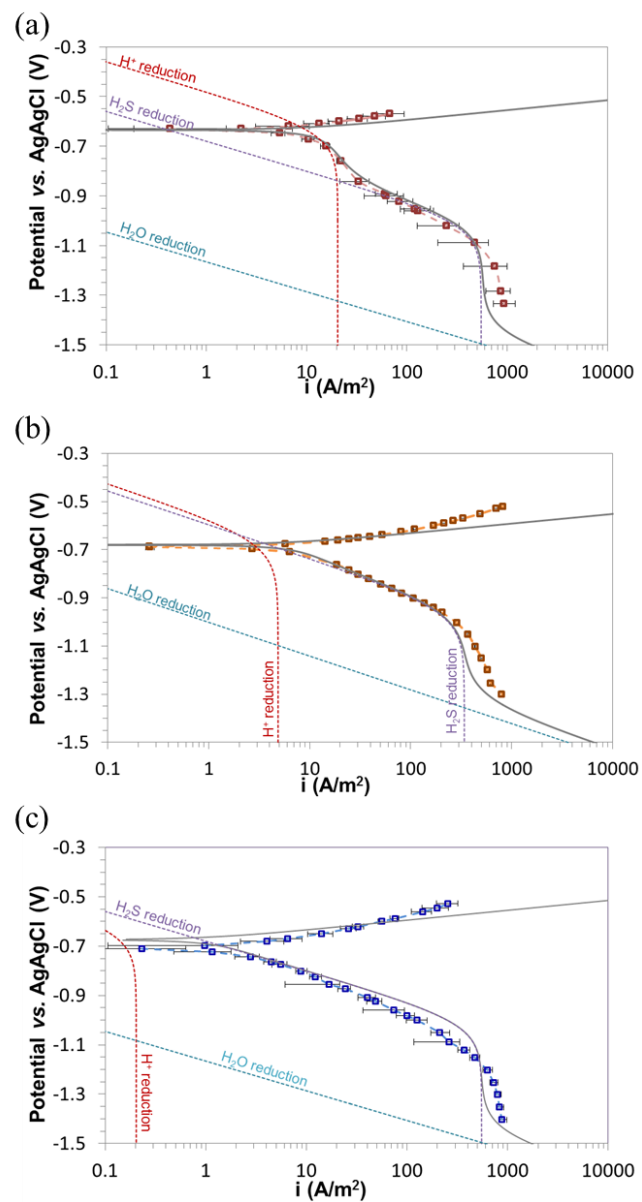


Figure 28. Potentiodynamic sweeps on mild steel in H_2S saturated solution with 0.096 MPa H_2S (960,000 ppm) in the gas phase, 3 wt. % NaCl, 30°C, and 1000 rpm RCE, scan rate 5 mV/s, (a) pH 3.0 (5 repeats); (b) pH 4.0 (4 repeats); (c) pH 5.0 (6 repeats).

3.4 Mixed CO₂ / H₂S Environment

3.4.1 Cathodic Reactions

There are four cathodic reactions in a mixed CO₂/H₂S aqueous system. The details of H⁺ reduction, H₂CO₃, H₂S reduction, and H₂O reduction have been described in previous chapters which covers these same reactions for a “pure” system, and no change is made for a mixed CO₂/H₂S aqueous system.

From experimental observation, it was found that when H₂S was present, the H₂O reduction rate was slowed down by approximately 1 or 2 orders of magnitude. Similarly, it is considered here that H₂CO₃ reduction was also slowed due to the presence of H₂S. In an H₂S environment, the i_0^{ref} for H₂CO₃ reduction was taken to be 0.0028 A/m² (4 times lower than the 0.014 A/m² used for a pure CO₂ environment without H₂S). The other parameters were taken to be the same as in the model without H₂S.

3.4.2 Anodic Reaction

The only anodic reaction: iron dissolution (65) and its kinetics are already presented above for pure systems.



This reaction is under charge transfer control. Thus, pure Tafel behavior can be assumed close to the corrosion potential.

$$i_{Fe} = i_{0,Fe} \times 10^{\frac{\eta}{b_a}} \quad (87)$$

When in a mixed H₂S/CO₂ environment, the anodic reaction rate is observed to mostly depend on H₂S concentration, as shown in Figure 29 and Figure 30. This behavior is modeled as proposed in 2.4, where the exchange current density is related to the

surface coverage by HS^- ions (θ_{HS^-}) and follows the Langmuir adsorption model, as Equation (83), (84) show.

$$i_{0,\text{Fe}} = i_{0,\text{Fe}}^{*} \theta_{\text{HS}^-} e^{\frac{\Delta H}{R} \left(\frac{1}{T} - \frac{1}{T_{\text{ref}}} \right)} \quad (83)$$

$$\theta_{\text{HS}^-} = \frac{K_2 c_{\text{HS}^-}}{1 + K_2 c_{\text{HS}^-}} \quad (84)$$

3.4.3 The Mixed Potential Theory

The corrosion potential then can be calculated by solving the charge balance Equation (88), which here takes the form:

$$i_{\text{Fe}} = i_{\text{H}_2\text{CO}_3} + i_{\text{H}_2\text{S}} + i_{\text{H}^+} + i_{\text{H}_2\text{O}} \quad (88)$$

Once the corrosion potential is found, the corrosion current and rate can be found from the anodic current (or total cathodic current) at the corrosion potential. The individual and total cathodic and anodic curves and predicted potentiodynamic sweeps can be generated, as is done in the steady state model of FREECORP™ 2.0 (similar to how it was done in FREECORP 1.0).

3.4.4 Model Verification

Performance of the model was validated by comparing the calculations with experimental results described above and with external data obtained from the open literature.

The effect of H_2S addition was simulated with the electrochemical model. Figure 29 and Figure 30 show the comparisons of simulated sweeps with experimental results at pH 4.0 and pH 5.0. Model simulations capture the changes of cathodic and anodic potentiodynamic sweeps with increasing H_2S gas concentration and generally agree with

experimental potentiodynamic sweeps at the different H₂S concentration. Figure 31 and Figure 32 show the corrosion rates calculated by the electrochemical model are in good agreement with experimental results, which all suggest the electrochemical model captures the main electrochemical processes underlying H₂S/CO₂ corrosion.

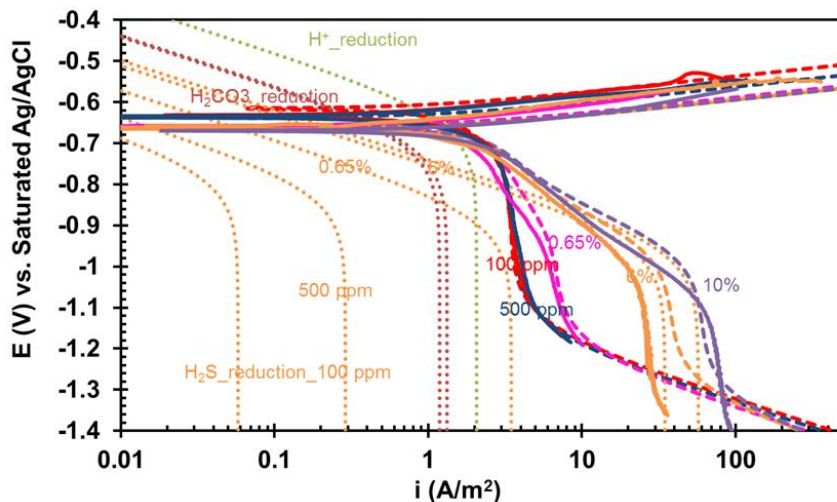


Figure 29. Comparison of predicted potentiodynamic sweeps with experimental results in the solution purged with different H₂S gas concentrations in the H₂S/CO₂ gas mixture at pH 4.0, 30°C, total pressure of 1 bar, 1 wt% NaCl, 1000rpm rotating speed, exposure time < 2 hours. Solid line: experimental sweeps, dashed line: predicted sweeps. Red: 100 ppm H₂S/CO₂, Dark blue: 500 ppm H₂S, pink: 0.65% H₂S, orange: 6% H₂S, purple: 10% H₂S in the H₂S/CO₂ gas mixture.

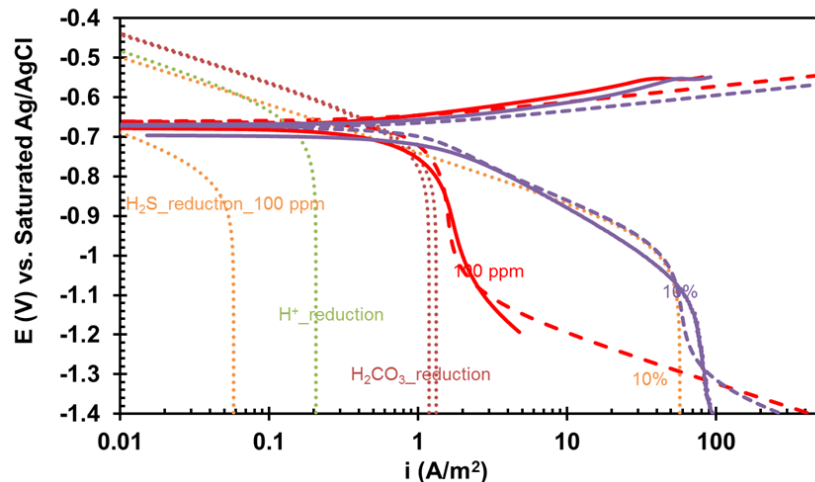


Figure 30. Comparison of predicted potentiodynamic sweeps with experimental results in the solution purged with different H_2S gas concentrations in the $\text{H}_2\text{S}/\text{CO}_2$ gas mixture at pH 5.0, 30°C, total pressure of 1 bar, 1 wt% NaCl, 1000rpm rotating speed, exposure time < 2 hours. Solid line: experimental sweeps. Dashed line: predicted sweeps. Red: 100 ppm H_2S , purple: 10% H_2S in the $\text{H}_2\text{S}/\text{CO}_2$ gas mixture.

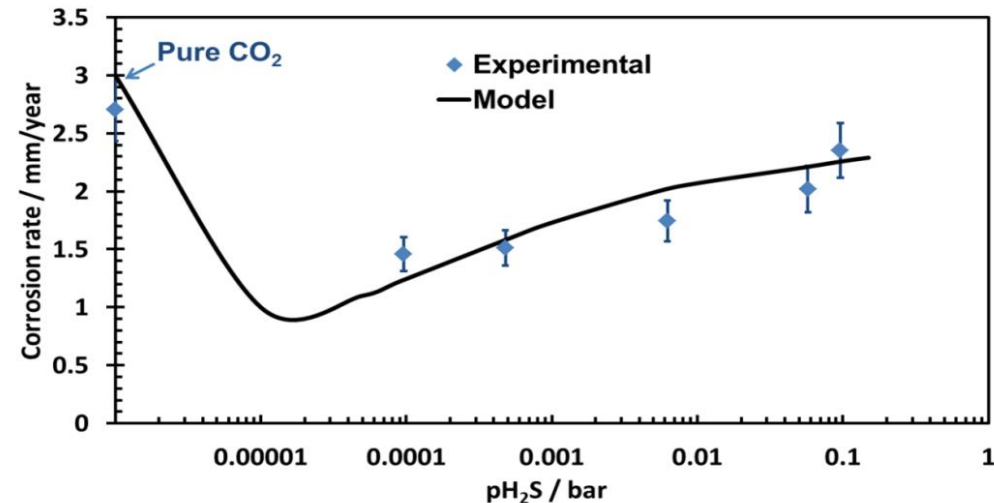


Figure 31. Comparison of corrosion rate predictions with experimental results in the solution purged with different H_2S gas concentrations in the $\text{H}_2\text{S}/\text{CO}_2$ gas mixture at pH 4.0, 30°C, total pressure of 1 bar, 1 wt% NaCl, 1000rpm rotating speed, exposure time < 2 hours.

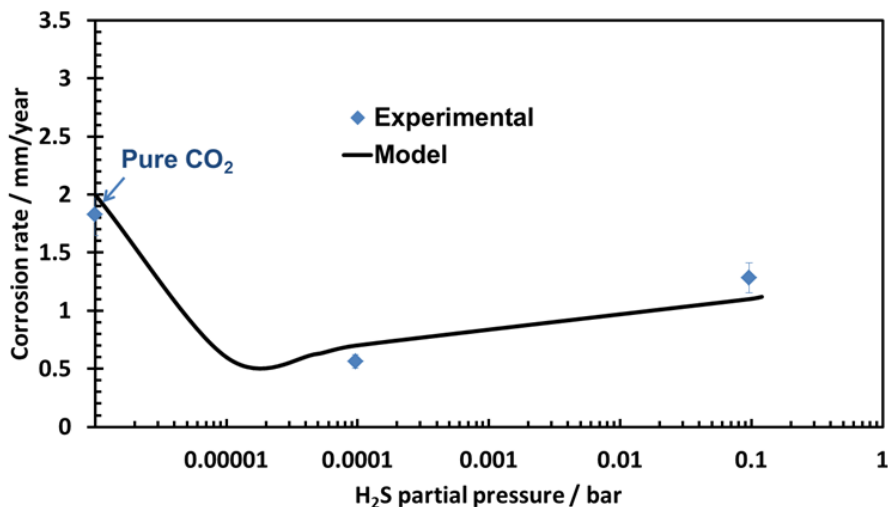


Figure 32. Comparison of corrosion rate predictions with experimental results in the solution purged with different H₂S gas concentrations in the H₂S/CO₂ gas mixture at pH 4.0, 30°C, total pressure of 1 bar, 1 wt% NaCl, 1000rpm rotating speed, exposure time < 2 hours.

The electrochemical model was also validated with external data obtained from the open literature. Model performance was examined first in low partial pressure of H₂S (pH₂S ranged from 0.05 mbar to 0.33 mbar, corresponding to 55 ppm to 340 ppm in the gas phase at 1 bar CO₂), where the experiments were conducted by Lee ²⁵. Figure 33 shows the corrosion rates change with H₂S partial pressure. It shows even a very low concentration of H₂S (50 ppm or 0.05 mbar) can reduce the CO₂ corrosion rate, which is greater than 1 mm/y in the absence of H₂S. The model clearly captures this effect.

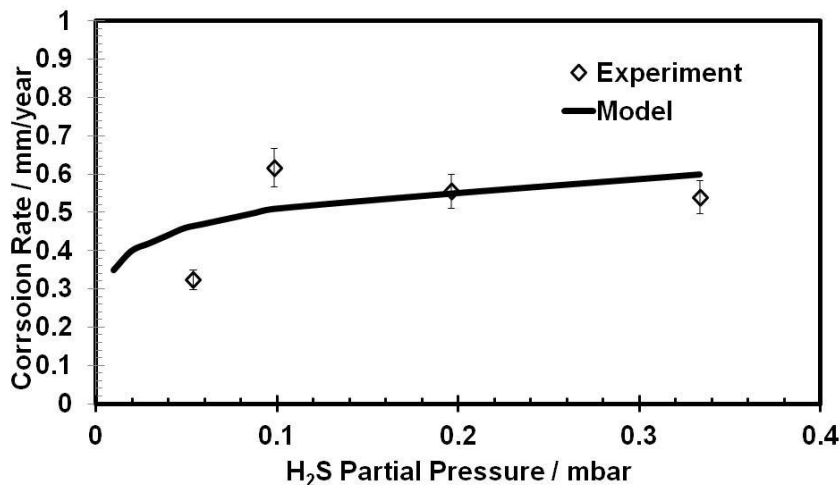


Figure 33. Comparison of corrosion rate predictions with experimental results in the solution purged with different partial pressures of H₂S gas in the H₂S/CO₂ gas mixture at total pressure of 1.0 bar, at pH 5.0, 20°C, 1 wt% NaCl, 1000 rpm, exposure time <1 h. Data taken from Lee ^{22 25}.

Corrosion experiments at a somewhat higher concentration of H₂S (pH₂S ranging from 1 mbar to 9.8 mbar, corresponding to 1000 ppm to 10,000 ppm H₂S in the mixed H₂S /CO₂ gas phase) was reported by Choi ²⁶. Model predictions are compared with the experimental results in Figure 34. Corrosion rates do not change much with H₂S concentration from 1 mbar to 9.8 mbar, which is broadly captured by the model.

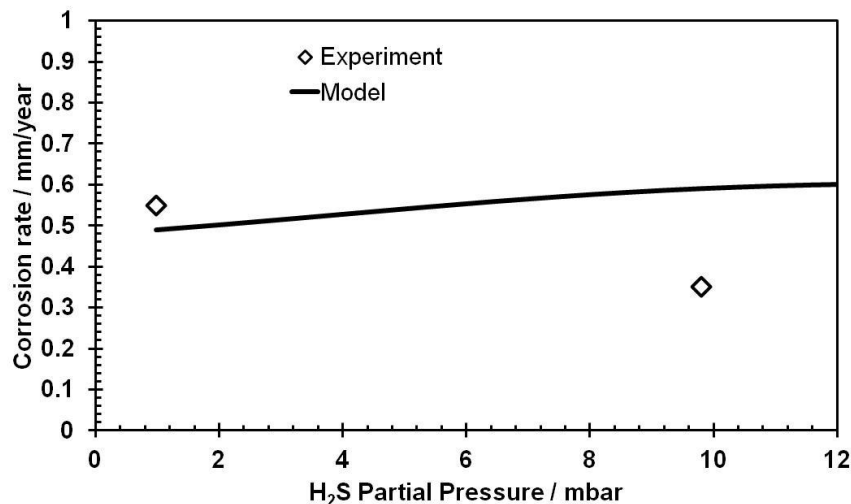


Figure 34. Comparison of corrosion rate predictions with experimental results in the solution purged with different partial pressures of H₂S gas in the H₂S/CO₂ gas mixture at total pressure of 1.0 bar, at pH 4.0, 25°C, 1 wt% NaCl, stagnant solution (0.01 m/s used in model), exposure time <1 hour. Data taken from Choi *et al.*²⁶.

The effect of temperature on corrosion rate was investigated by Abayarathna *et al.*²⁷ where corrosion rates increased with temperature at different H₂S concentration conditions. The experiments were simulated using the present CO₂/H₂S model and it was found that the model can predict the measured corrosion rate change, as shown in Figure 35.

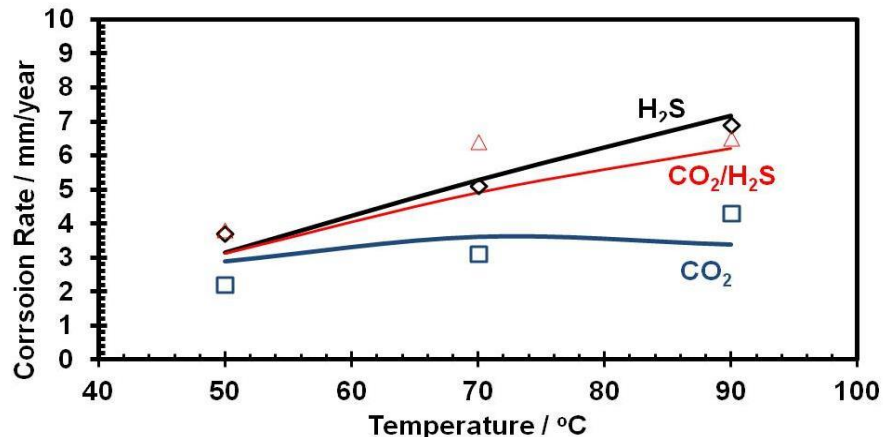


Figure 35. Comparison of corrosion rate predictions with experimental results for different temperatures; experimental data shown as points, model predictions shown as lines; total pressure = 1 bar, exposure <1 hour, pH 4.2 (4.5 at 90°C, CO₂), stirring condition. Assumed model parameters: volume ratio for mixture CO₂/H₂S=1:1, flow velocity 0.3 m/s. Data taken from Abayarathna *et al.*²⁷.

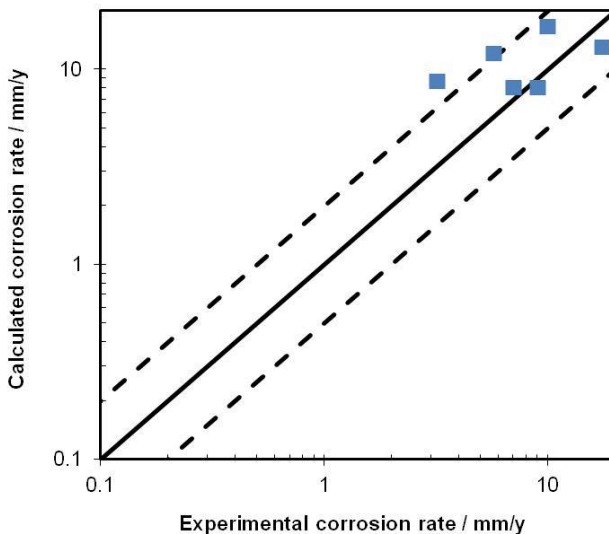


Figure 36. Parity plot showing a direct comparison of predicted and experimental corrosion rates; data taken from Bich and Goerz²⁸, pCO₂ = 3 bar to 12.8 bar, pH₂S = 3 bar to 12.2 bar, pH 5.0, v = 0.1 m/s. The solid line represents perfect agreement of experimental and calculated corrosion rates. The dashed lines represent a factor of 2 deviation.

A corrosion case at more severe conditions was reported by Bich and Goerz²⁸. The experimental condition includes high partial pressures of CO₂ (pCO₂ = 3 bar to 12.8 bar) and H₂S (pH₂S = 3 bar to 20 bar). The predicted corrosion rates are within a factor of 2 of the measured data points as Figure 36 shows.

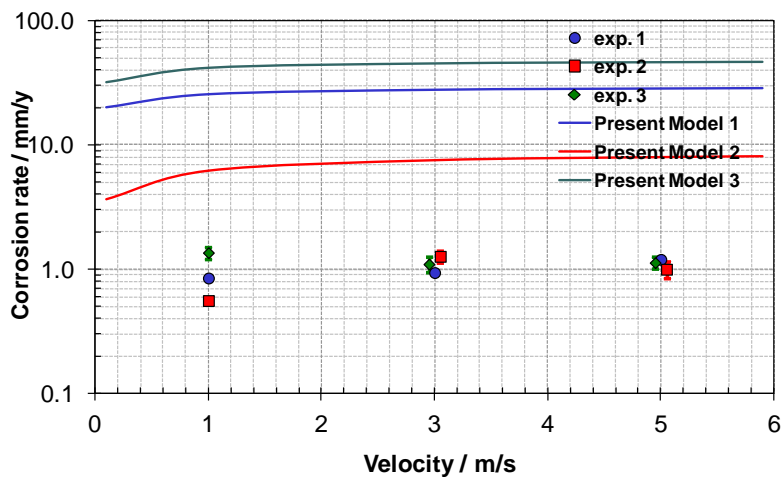


Figure 37. Comparison of corrosion rate predictions with experimental results for different velocities; experimental data shown as points, present electrochemical model predictions shown as lines; exp. 1: 19 days, $p = 40$ bar, $p\text{CO}_2 = 3.3$ bar, $\text{pH}_2\text{S} = 10$ bar, 80°C , pH 3.5, $v = 1$ m/s to 5 m/s; exp. 2: 21 days, $p = 40$ bar, $p\text{CO}_2 = 3.3$ bar, $\text{pH}_2\text{S} = 10$ bar, 25°C , pH 3.5, $v = 1$ m/s to 5 m/s; exp. 3: 10 days, $p = 40$ bar, $p\text{CO}_2 = 10$ bar, $\text{pH}_2\text{S} = 30$ bar, 80°C , pH 3.2, $v = 1$ m/s to 5 m/s; experimental data taken from Omar, *et al.*²⁹.

Long-term flow loop experiments (15 – 21 days) at high partial pressure of H_2S ($\text{pH}_2\text{S} = 10$ bar to 30 bar) and high partial pressure of CO_2 ($p\text{CO}_2 = 3.3$ bar to 10 bar) was conducted by Omar, *et al.*²⁹. Figure 37 shows a comparison between the present electrochemical model prediction and experimental results. The model over-predicts the corrosion rate by a large factor, by 10 to 50. This is due to the formation of iron sulfide layers on the surface, which are not accounted for in the current model. Sun and Nešić's mass transfer based model³¹

considers the effect of iron sulfide corrosion product layers and makes a better prediction for long term experiments, as Figure 38³⁰ shows. Further extension of the current electrochemical model to include mass transfer effects and coverage effect due to iron sulfide layer formation.

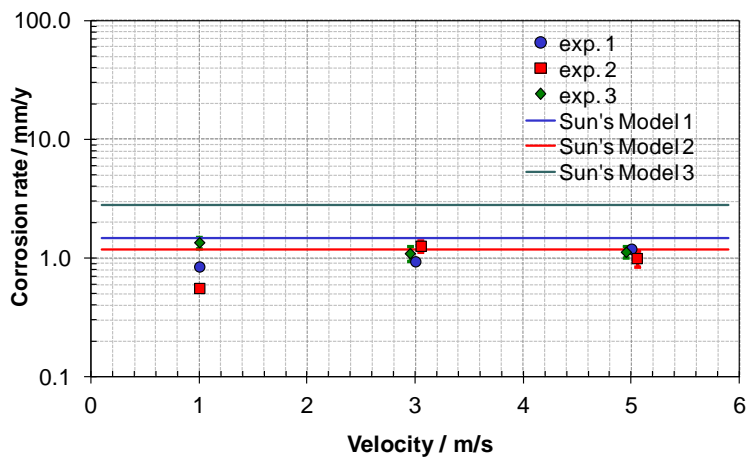


Figure 38. Comparison of corrosion rate predictions with experimental results for different velocities; experimental data shown as points, Sun and Nešić's mass transfer model (Sun's model) predictions shown as lines; exp. 1.: 19 days, $p = 40$ bar, $p\text{CO}_2 = 3.3$ bar, $\text{pH}_2\text{S} = 10$ bar, 80°C , pH 3.5(calculated), $v = 1$ m/s to 5 m/s; exp. 2.: 21 days, $p = 40$ bar, $p\text{CO}_2 = 3.3$ bar, $\text{pH}_2\text{S} = 10$ bar, 25°C , pH 3.5 (calculated), $v = 1$ m/s to 5 m/s; exp. 3.: 10 days, $p = 40$ bar, $p\text{CO}_2 = 10$ bar, $\text{pH}_2\text{S} = 30$ bar, 80°C , pH 3.2 (calculated), $v = 1$ m/s to 5 m/s; experimental data taken from Omar, *et al.*²⁹.

3.5 Aqueous Environment in the Presence of Organic Acids

3.5.1 Cathodic Reactions

Similar to the case of carbonic acid corrosion, increased corrosion rates in the presence of acetic acid is due to its direct reduction at the metal surface. Therefore, the most influential factor is the concentration of the undissociated (“free”) acetic acid and not the acetate ion. One can appreciate that the organic acids are a major corrosion concern primarily at lower pH values.

Direct HAc reduction is represented by:



The acetic acid reduction reaction (90) can be either under charge transfer or mass transfer (diffusion) control, therefore acetic acid reduction rate can be calculated as:

$$\frac{1}{i_{HAc}} = \frac{1}{i_{\alpha,HAc}} + \frac{1}{i_{lim,HAc}^d} \quad (90)$$

The charge transfer current density is given as:

$$i_{\alpha,HAc} = i_{0,HAc} \times 10^{-\frac{\eta}{b_c}} \quad (91)$$

where $i_{0,HAc}$ is the exchange current density (A/m^2), b_c is the cathodic Tafel slope (V/decade), η is the over potential (V), which is equal to the difference between the operating (actual) potential and the reversible potential.

The cathodic Tafel slope b_c and reversible potential can be calculated from:

$$b_c = \frac{2.303RT}{\alpha_c F} \quad (92)$$

$$E_{rev} = -\frac{2.303RT}{F} pH - \frac{2.303RT}{2F} \log p_{H_2} \quad (93)$$

where $\alpha_c = 0.5$ giving $b_c \approx 0.120 \text{ V/decade}$ at 30°C .

The exchange current density can be calculated by:

$$i_{0,HAc} = i_{0,HAc}^{ref} \left(\frac{c_{HAc}}{c_{HAc}^{ref}} \right)^{0.5} \times e^{-\frac{\Delta H_{HAc}}{R} \left(\frac{1}{T} - \frac{1}{T_{ref}} \right)} \quad (94)$$

the i_{0ref} for HAc reduction was taken to be 0.04 A/m^2 at 293.15K reference temperature and 0.00142 mol/L reference HAc concentration. The enthalpy of activation in Equation (94) is set to 55 kJ/mol .

The diffusion limiting current in Equation (90) is calculated as:

$$i_{lim,HAc}^d = k_{m,HAc} F c_{HAc} \quad (95)$$

where $k_{m,HAc}$ represents HAc mass transfer coefficient (m/s) and c_{HAc} represents the bulk concentration of HAc (mol/L).

The mass transfer coefficient of HAc can be calculated from mass transfer correlations, presented above.

3.5.2 *Anodic Reaction*

There are no changes in how the rate of the anodic reaction is calculated, compared to what was presented above.

3.5.3 *The Mixed Potential Theory*

The corrosion potential then can be calculated by solving the charge balance equation:

$$\sum i_a = \sum i_c \quad (96)$$

which here takes the form:

$$i_{Fe} = i_{HAc} + i_{H_2CO_3} + i_{H_2S} + i_{H^+} + i_{H_2O} \quad (97)$$

Once the corrosion potential is known, the corrosion current and rate can be found from the anodic current (or the sum of cathodic currents) at the corrosion potential. The individual and total cathodic and anodic curves, and predicted potentiodynamic sweeps can be then readily generated, as done in the steady state model of FREECORP™ 2.0 (similar to how it was done in FREECORP 1.0).

3.5.4 *Model Verification*

The effect of HAc is particularly pronounced at higher temperatures and low pH when the abundance of undissociated HAc can increase the CO_2 corrosion rate dramatically as seen in Figure 39. Solid iron acetate does not precipitate in the pH range

of interest since iron acetate's solubility much higher than that of ferrous carbonate. There are some indications that the presence of organic acids impairs the protectiveness of ferrous carbonate layers, however the mechanism is still not clear.

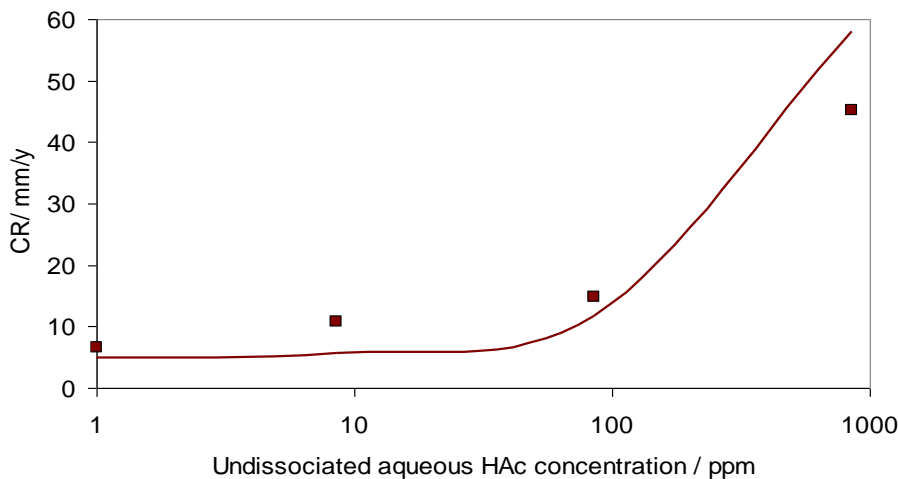


Figure 39. The effect of the concentration of undissociated acetid acid (HAc) on the CO₂ corrosion rate, 60°C, $P_{CO_2}=0.8$ bar, pH4, 12 mm OD rotating cylinder flow at 1000 rpm. Experimental data taken from Geroge and Nešić et al.³⁰

3.6 Model Limitations

The key limitation of this steady state electrochemical corrosion model are:

- The current model covers only uniform carbon steel corrosion. It does not address localized corrosion.
- The calculation of rates of the various electrochemical processes underlying corrosion is done by referencing the bulk water chemistry conditions which can be quite different form the water chemistry at the corroding steel surface. The former is much easier to implement while the latter is more correct. This correction has been implemented in the transient model described in the following chapter.

- The model does not include the formation of solid corrosion product layers on the surface of the steel, which can be protective. This effect is covered by the transient model described below.
- This is a steady state models so any changes in time that occur for any reason are not considered. This is also addressed by the transient model described below.
- A simple water chemistry was considered in the current model, which means that the infinite solution theory and an ideal solution are assumed. Concentrations of different species are used rather than activities.
- Empirical mass transfer correlations are used to account for the mass transfer process, making it only take into account the effect of single-phase pipe flow. When available, empirical mass transfer correlations for different flow geometries (e.g. rotating cylinder, rotating disc, impinging jet, et.) or those applying in multiphase flow, can be used with the current model.
- The effects of high salt concentrations, oxygen, elemental sulfur and other complicating factors in the corrosion process are not considered in the current model.

CHAPTER 4. TRANSIENT MODEL

The transient model with corrosion product layer growth built into FREECORPTM 2.0 is based on similar electrochemical foundations as the steady state model described above, however, it also accounts for the protectiveness of corrosion product layers. Furthermore, all the electrochemical kinetic parameters are based on surface water chemistry, rather than the bulk.

This model has some similarities but also many important differences when compared to the equivalent model that was built into FREECORP 1.0. A comparison between the two models is listed in Table 7.

Table 7. Comparison between FREECORP 1.0 and FREECORPTM 2.0 transient model with corrosion product layer growth

FREECORP 1.0	FREECORP TM 2.0
No mechanistic iron carbonate corrosion product layer growth, a factor used instead	Fully mechanistic transient model of iron carbonate corrosion product layer growth
Accounts for an inner 1-10 nm thin mackinawite film acting as a solid state diffusion barrier.	Accounts for a thin adsorbed iron sulfide film affecting the kinetics of different electrochemical reactions (retardation effect).
Accounts for porous outer iron sulfide layer formation by spalling of the thin inner mackinawite film.	Accounts for a porous outer iron sulfide layer formation via a precipitation mechanism.
Corrosion rate is always under mass-transfer control due to the porous outer and inner iron sulfide layers.	Corrosion rate is not always under mass-transfer control, it depends on the environmental conditions, accounted for by the mechanistic coupling of mass transfer and electrochemical reactions.

Before details of the model are presented a brief introduction of iron carbonate and iron sulfide corrosion product layers is given.

4.1 Iron Carbonate and Iron Sulfide

Long term corrosion experienced in lab and field conditions is dominated by the formation of corrosion product layer. Corrosion product layer can form a diffusion barrier

for the corrosive species and, when well attached to the steel surface, and significantly reduce the rate of electrochemical reactions and consequently the rate of general corrosion. However, not every corrosion product layer formed in reality is protective. Parameters that affect the protectiveness of corrosion product layer will be explained below.

As the most common corrosion product in aqueous CO₂ corrosion of mild steel, FeCO₃ could precipitate from solution through the precipitation reaction (98) depending upon the saturation level of FeCO₃:



The saturation level of FeCO₃ is defined by

$$S_{FeCO_3} = \frac{c_{Fe^{2+}} \cdot c_{CO_3^{2-}}}{K_{sp,FeCO_3}} \quad (99)$$

in which the solubility product, $K_{sp,FeCO_3}$ in (mol/L)², is a function of temperature and ionic strength as defined by the following equation ³²

$$K_{sp,FeCO_3} = [c_{Fe^{2+}}]_{eq} [c_{CO_3^{2-}}]_{eq} \quad (100)$$

where the subscript “eq” refers to the equilibrium aqueous concentrations of Fe^{2+} and CO_3^{2-} . In an aqueous CO₂ environment, FeCO₃ precipitates if the concentration product of $c_{Fe^{2+}} \cdot c_{CO_3^{2-}}$ exceeds the solubility product, $K_{sp,FeCO_3}$, i.e., when $S_{FeCO_3} > 1$. The precipitated FeCO₃ dissolves from the surface when $S_{FeCO_3} < 1$. Therefore, the saturation value can be used to determine if a FeCO₃ layer forms or not.

In an aqueous H₂S corrosion environment, we make a distinction between two different types of FeS layers formed on the steel surface. The so called “inner” FeS film

of mackinawite is very thin and immediately adjacent to the steel surface, and formed via a rapid chemisorption process, *i.e.*, by a direct reaction of surface Fe with H₂S. The outer, often much thicker, layer of FeS is formed by precipitation from the aqueous solution onto the initially formed thin layer of mackinawite. This outer layer is not always found and depends on the surface water chemistry. Similar to FeCO₃, the formation of this outer FeS layer depends on the saturation value for iron sulfide. The precipitation reaction for iron sulfide is:



The saturation value for iron sulfide formation is calculated by:

$$S_{FeS} = \frac{c_{Fe^{2+}} c_{S^{2-}}}{K_{sp, S^{2-}}} \quad (102)$$

and the $K_{sp, S^{2-}}$ is the solubility product of FeS in (mol/L)².

The protective properties for both types of corrosion product layer is also related to the corrosion rate of steel underneath. This relationship is best expressed via the concept of surface scaling tendency (SST), which describes the relative rate of precipitation with respect to corrosion rate (undermining rate) at the steel surface, expressed in the same volumetric units, as shown by:

$$SST = \frac{\text{Precipitation Rate (PR)}}{\text{Corrosion Rate (CR)}} \quad (103)$$

When $SST \geq 1$, the rate of precipitation at the steel surface equals or exceeds the rate of corrosion (termed “undermining”), the condition is favorable for formation of dense, protective corrosion product layers which can cause corrosion rate reduction. Vice versa, when $SST < 1$, the corrosion process undermines the newly formed corrosion

product layer faster than precipitation can fill in the voids. A porous and non-protective layer forms, which can be very thick. Generally, the thickness of corrosion product layer plays a lesser role in corrosion rate retardation than do the density and proper attachment of the layer to the steel surface.

The balance between corrosion product precipitation and the undermining process can lead to a variety of corrosion outcomes and depends on environmental parameters such as temperature, pH, and flow rate. The protective corrosion product layer and low corrosion rates were observed at high pH, temperature and low flow rate due to formation of dense corrosion product layers. The concept of scaling tendency is a good predictor for formation of protective corrosion product layers.

4.2 Model Construction

The transient model with corrosion product layer growth built into FREECORPTM 2.0 has three main parts:

- (1) a water chemistry model in the bulk solution, which is the same as the one for the steady state model described above,
- (2) an electrochemical corrosion model, which is similar to what was shown above but is based on surface water chemistry conditions, including mass transport calculations from bulk to the steel surface, and
- (3) a corrosion product layer growth model including iron carbonate and iron sulfide.

4.2.1 Bulk Water Chemistry Model

This model is identical to the one presented in Chapter 2 above.

4.2.2 *Electrochemical Corrosion Model*

This electrochemical model is based on surface water chemistry conditions, which are generally unknown. Therefore, two computational locations were distinguished in the computational domain covering the mass transfer boundary layer in the aqueous solution (called “nodes” in the text below): one in the bulk solution and the other in the thin water layer adjacent to the steel surface (called “surface water layer” in the following text). The equilibrium concentrations of different chemical species in the bulk solution can be readily calculated, as shown in Chapter 2. The calculation node for the bulk solution did not require any modification from what is shown there. However, calculating the concentrations of species at the second node at the surface water layer needs to be addressed differently to properly account for the different physicochemical processes that govern them. They are summarized in Figure 40, and can be listed as follows:

- Homogenous chemical reactions in the surface water layer (the same ones as in the bulk).
- Electrochemical reactions at the steel surface, which cause the flux of various species in or out of the surface water layer.
- Transport of species to and from the bulk, including convection and diffusion through the boundary layer as well as migration due to establishment of potential gradients in the solution.

These three physicochemical processes can be accounted for by writing a material balance (mass conservation equation) for aqueous species j in the surface water layer.

$$\frac{\partial c_{\text{surface}, j}}{\partial t} = \frac{N_{in,j} - N_{out,j}}{\Delta x} + R_j \quad (104)$$

where $c_{\text{surface}, j}$ is the concentration of species j ; R_j the source term (production/destruction) of species j due to homogeneous chemical reactions involving species j ; $N_{in,j}$ is the flux of species j due to mass transfer from the bulk solution to the surface water layer by diffusion, convection and electromigration. $N_{out,j}$ is the flux of species j due to electrochemical reactions at the steel surface (zero for non-electrochemical species).

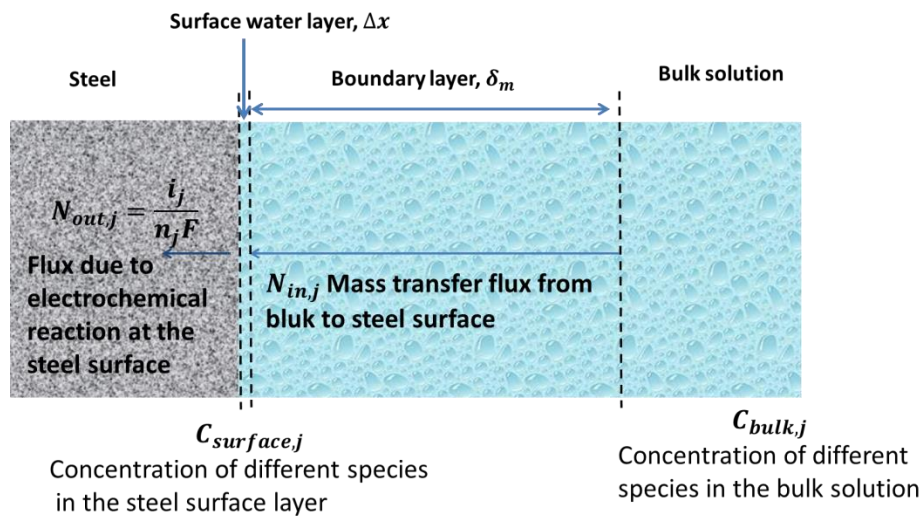


Figure 40. Illustration of computation domain for mass balance calculations.
 4.2.2.1 Homogenous Chemical Reaction Rate R_j

The homogenous reactions included in the current model are all listed in Table 1 and Table 3. The equilibrium constants needed to determine species dissociation are listed in Table 2 and Table 4.

It should be noted that chemical reactions are often very rapid compared to other processes involved in corrosion, such as species transport from the bulk solution to the steel surface and electrochemical reactions at the steel surface, thus preserving chemical equilibria throughout the solution. This was taken advantage of in the steady state electrochemical model presented in Chapter 3. On the other hand, in the case of slow chemical reactions (such as for example the CO₂ hydration reaction (3)), other faster processes can lead to local non-equilibrium conditions in the surface water layer. Therefore, chemical reactions can significantly affect the rates of electrochemical processes at the steel surface and the ultimately – the corrosion rate. In order to better understand how the rates of homogenous chemical reactions are calculated, one can refer to Nesic, *et al.*³⁴. An example is shown here using for example the H₂S dissociation chemical reaction.



Then the net chemical reaction rate for HS⁻ species can be expressed as the equation below.

$$R_{hs} = k_{f,hs}c_{H_2S} - k_{b,hs}c_{H^+}c_{HS^-} \quad (105)$$

where $k_{f,hs}$ is the “forward” kinetic constant for the dissociation reaction and $k_{b,hs}$ is the “backward” kinetic constant for the same reaction. This rate will be involved in the mass balance for the steel surface layer, along with the other fluxes.

4.2.2.2 *Electrochemical Reaction Rates and the flux $N_{out,j}$ at the Steel Surface*

Electrochemical reactions considered in the transient model are the same ones as described in Chapter 3. Just like there, the Tafel equation is used to calculate the current densities (rate) of various electrochemical reactions.

In this model, the current density for each electrochemical reaction depends on the surface concentration of species, which is not explicitly known and needs to be calculated, as explained further below. For a spontaneous corrosion process, the unknown corrosion (mixed) potential of the steel, E can be calculated from the charge balance equation at the steel surface as explained in Chapter 3. Once the corrosion potential (E) is found, the partial current (i_j) for a given species j is readily found and the flux of species j due to an electrochemical reaction at the steel surface can be calculated from Faraday's law:

$$N_{out,j} = \pm \frac{i_j}{n_j F} \quad (106)$$

where n_j is the number of moles of electrons exchanged per mol of species j participating in a given electrochemical reaction. For species j consumed by electrochemical reactions at the steel surface, the positive sign is applied. For species j produced by electrochemical reactions at the steel surface, the negative sign is applied. For those species j that are not involved in the electrochemical reactions $N_{out,j}=0$.

4.2.2.3 *Species Surface Concentration and Mass Transfer Flux $N_{in,j}$ Between the Bulk and Steel Surface*

Ten (10) minor species (H_2S , HS^- , S^{2-} , CO_2 , H_2CO_3 , HCO_3^- , CO_3^{2-} , OH^- , H^+ , Fe^{2+}) and two (2) major species (Na^+ and Cl^-) were considered to calculate the mass transfer flux from the bulk solution to the surface water layer. Any homogenous chemical

reactions in the water solution between the bulk solution and the surface water layer are not accounted for in this model. It is assumed that the change in concentration for each species is linear over this region with the slope defined by the mass transfer coefficient ($k_{m,j}$) of species j .

The mass transfer flux from the bulk solution to the surface water layer can be calculated for each of the minor species as:

$$N_{in,j} = k_{m,j} * (c_{bulk,j} - c_{surface,j}) \quad (107)$$

Here $c_{bulk,j}$ is the known equilibrium concentration of the species in the bulk solution, $c_{surface,j}$ is the concentration of the species in the surface water layer, $k_{m,j}$ is the mass transfer coefficient. The mass transfer coefficient can be calculated from well-known hydrodynamic relations among Re, Sc and Sh number as shown in Chapter 3.

For the major species (Na^+ and Cl^-), ion electro-migration needs to be considered which adds an additional term to the equation for mass transfer flux from the bulk solution to the surface water layer:

$$N_{in,j} = k_{m,j} * (c_{bulk,j} - c_{surface,j}) + k_{m,j} * \frac{z_j F}{RT} c_{bulk,j} \Delta\Phi \quad (108)$$

Here, z_j is the electric charge of the species, $\Delta\Phi$ represents a small electrical potential difference between the bulk solution and the surface water layer. The bulk concentration $c_{bulk,j}$ is used in the second (electromigration) term on the right to make the equation explicit and linear. Actually the average value of the bulk and surface concentrations should be used, but this difference is very small and can be assumed to be

negligible (of the order of the concentration of minor species) due to an excess of supporting electrolyte.

4.2.2.4 *The Mass Conservation Equations*

Substitution of flux density due to electrochemical reactions and mass transfer processes into mass conservation equation of Equation (104) yields Equation (109) for the minor species:

$$\Delta x \frac{\partial c_{surface,j}}{\partial t} = -\frac{i_j}{n_j F} + k_{m,j} * (c_{bulk,j} - c_{surface,j}) + \Delta x * R_j \quad (109)$$

For the major species, this same procedure yields (110):

$$\Delta x \frac{\partial c_{surface,j}}{\partial t} = k_{m,j} * (c_{bulk,j} - c_{surface,j}) + k_{m,j} * \frac{z_j F}{RT} c_{bulk,j} \Delta \Phi \quad (110)$$

There are 13 unknowns (10 unknown surface minor species concentrations, 2 unknown surface major species concentrations and 1 unknown potential $\Delta\Phi$), but only 12 mass conservation equations were formulated above. One more equation is needed. Since the aqueous solution is assumed to be charge neutral, the electro-neutrality equation must be followed:

$$\sum z_j c_{surface,j} = 0 \quad (111)$$

Therefore, the concentration for all the chemical species in the surface water layer can be calculated from these 13 equations. At the same time, corrosion current, the corrosion potential, corrosion rate, and the rates (currents) for each of the electrochemical reactions can also be calculated from their corresponding Tafel equations.

From the description above, it appears that the equations for the minor species are independent from the equations for the major species and the electrical potential. According to Newman³⁵

, the first step should be to solve the equations for the concentrations of the minor species in the solution and then, secondly, to solve the equations for the concentrations of the major species and the electrical potential gradient $\Delta\Phi$.

4.2.2.5 Numerical Implementation

Theoretically the 13 equations can be readily solved, but there are two numerical difficulties that need to be addressed. First, the equations for the minor species are highly non-linear due to the presence of chemical reactions term, by which various species concentrations are linked together.

In the example above, the non-linear term arises from the multiplication of two concentrations, e.g. $k_{b,hs}c_{H^+}c_{HS^-}$ shown above. In more advanced mechanistic models such MULTICORPTM, the nonlinear chemical reaction rates are linearized by using a Taylor series expansion around the known solution concentrations in the previous time step. Actually, if the concentration of c_{H^+} is known, then all of the chemical reaction terms become linear. Therefore, one of the most stable calculation methods, the bisection method, was used in the current model to find a c_{H^+} value to satisfy the equations. The details of the calculation process are shown in Zheng's dissertation³⁶.

The second numerical difficulty is related to the magnitude of the chemical reaction rate constants, which make the set of equations "stiff" i.e. difficult to solve. In MULTICORPTM, this issued is also solved by using linearized Taylor series expansion around the known solution in the previous time step and by keeping only the constant and the linear term. Pots³⁷ proposed two alternative ways to resolve these issues in his CO₂ corrosion model. One way was to decrease the chemical reaction rate, but keep it faster than the other processes. An alternative way was to calculate the concentrations of HCO₃⁻,

CO_3^{2-} , and OH^- directly from the equilibrium constants and then calculate the H^+ concentration from the charge electro-neutrality equation. All the carbonic species (H_2CO_3 , HCO_3^- , and CO_3^{2-}) are then lumped together into one mass transport equation. In the current model, a method similar to this second method proposed by Pots³⁷ was used.

For the sulfide species group (H_2S , HS^- , and S^{2-}), three mass conservation equations were developed. Because chemical reaction rates for the first and second dissociation of H_2S are fast, these three mass conservation equations can become one mass conservation equation for total sulfide species and two more chemical equilibria equations. Therefore, chemical reaction rate terms vanish from the mass balance equations. A similar strategy was used for carbonic species (aqueous CO_2 , H_2CO_3 , HCO_3^- , and CO_3^{2-}), but because CO_2 hydration is a slow reaction, the mass conservation equation for the aqueous CO_2 species must be kept. Therefore, four mass conservation equations for aqueous CO_2 , H_2CO_3 , HCO_3^- , and CO_3^{2-} become one mass conservation equation for all aqueous carbonic species, one mass conservation equation for aqueous CO_2 , and two more chemical equilibria equations for carbonic acid dissociation and bicarbonate ion dissociation. For H^+ and OH^- species, two mass conservation equations become two new equations. One is obtained by substituting all the chemical reaction rate terms with the expression from other mass conservation equations to a H^+ species mass conservation equation. The other is the chemical equilibria equation for H_2O dissociation.

4.2.3 Corrosion Product Layer Growth Model

From the previous electrochemical corrosion model, the surface water chemistry (the concentration of different chemical species at the steel surface) can be obtained. Based on the concentrations of different species at the steel surface, a thermodynamic model based on research by Ning⁸ and Tanupabrungsun³⁸ can be used to predict which solid corrosion product should form on the steel surface. If no solid corrosion product is expected to form, the corrosion process will continue to occur unimpeded. If a corrosion product layer forms on the steel surface, the growth and morphology of the corrosion product layer will affect the corrosion process. Therefore, a corrosion product layer growth model, which focuses on kinetics of iron carbonate and iron sulfide formation, was developed to address these issues.

In the previous electrochemical corrosion model at section 4.2.2, two distinct computational locations (nodes) were considered: one at the steel surface water layer and one in the bulk solution. Because of the corrosion product layer, one more node needs to be added for the corrosion product layer, as shown in Figure 41. This enables addition of an additional physicochemical process: corrosion product growth to the three previously considered physicochemical processes: chemical reactions, electrochemical reactions, and mass transport.

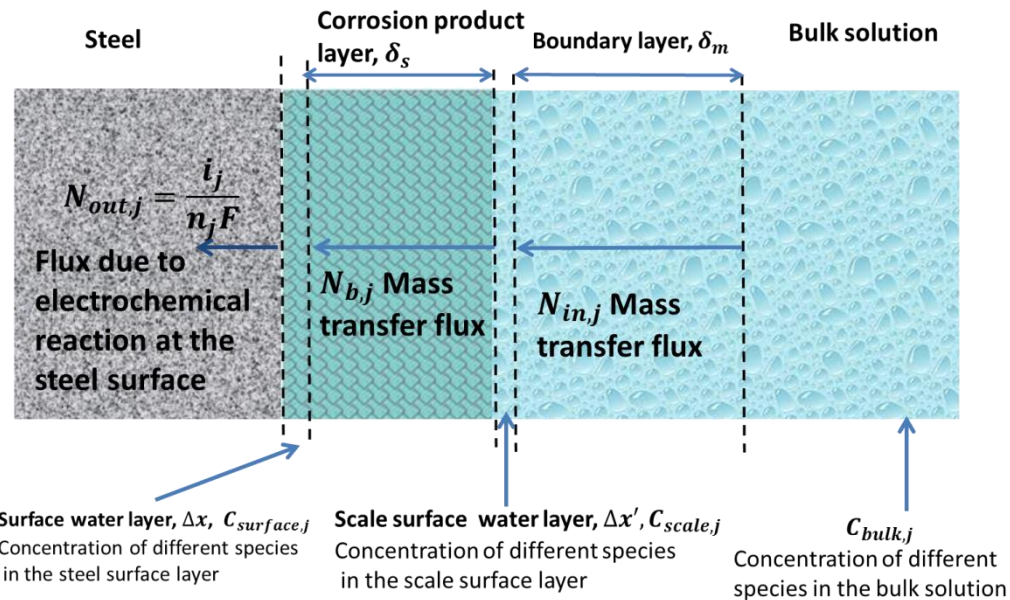


Figure 41. Sketch of corrosion process with corrosion product layer.

The slightly modified mass conservation equation for the corrosion product layer is:

$$\frac{\partial \varepsilon c_{surface,j}}{\partial t} = \frac{N_{b,j} - N_{out,j}}{\Delta x} + R_j \quad (112)$$

here, ε is the porosity of the corrosion product layer, R_j is the source term due to the production or consumption of species j due to chemical reactions involving species j (this includes homogeneous chemical reactions described above, as well as heterogeneous chemical reactions such as iron sulfide precipitation and/or iron carbonate precipitation. $N_{b,j}$ is the flux of species due to mass transfer from the porous corrosion product layer to the surface water layer adjacent to it and $N_{out,j}$ is the flux of species due to electrochemical reactions at the steel surface, which are affected by the coverage of the

surface by the corrosion product layer. How these three terms, R_j , $N_{b,j}$ and $N_{out,j}$ are affected by the presence and growth of the corrosion product layer is addressed below.

4.2.3.1 Heterogeneous Chemical Reactions

Homogenous reactions in the surface water layer and bulk water locations have been addressed in the previous sections. In the porous corrosion product layer, they are treated very similarly as in the surface water layer. The main focus here is to deal with two new heterogeneous chemical reactions: solid iron carbonate formation and solid iron sulfide formation.

4.2.3.1.1 Iron Carbonate Formation

Iron carbonate precipitation acts as a sink for Fe^{2+} and CO_3^{2-} . When saturation of iron carbonate, as defined in (99), is higher than 1, net iron carbonate precipitation occurs and consumes Fe^{2+} and CO_3^{2-} .

Equation (113) describes the kinetics of iron carbonate precipitation proposed by Sun, *et al.*³⁹, which is used in the present model.

$$R_{\text{FeCO}_3(s)} = e^{28.20 - \frac{64.85}{RT}} \frac{S}{V} K_{sp\text{FeCO}_3} (S_{\text{FeCO}_3} - 1) \quad (113)$$

where $R_{\text{FeCO}_3(s)}$ is the precipitation rate in $\text{mol/m}^3\cdot\text{s}$; $\frac{S}{V}$ is the surface volume ratio of the iron carbonate in $1/\text{m}$. $K_{sp\text{FeCO}_3}$ represents the solubility limit of iron carbonate in $(\text{mol/L})^2$, which is given by Equation (114)³⁹.

$$\log K_{sp\text{FeCO}_3} = -59.3498 - 0.041377T - \frac{2.1963}{T} + 24.5724\log T + 2.518I^{0.5} - 0.657I \quad (114)$$

where T is the temperature in K and I is the ionic strength in mol/L.

4.2.3.1.2 Iron Sulfide Formation

The iron sulfide layer forms when the product of the concentrations of Fe^{2+} and S^{2-} ions exceeds the solubility limit according to reaction (101).

The precipitation kinetics is much faster for iron sulfide than for iron carbonate and the solubility for iron sulfide is much lower than iron carbonate. So in the current model, when it is determined from water chemistry that an iron sulfide layer can precipitate ($S_{\text{FeS}} > 1$), iron carbonate precipitation is ignored. Although some research can be found^{40, 41}, on the precipitation kinetics of iron sulfide, no reliable expression for the precipitation kinetics of iron sulfide has been developed. A new expression is developed, which is similar to the iron carbonate precipitation kinetics:

$$R_{\text{FeS}(s)} = e^{A - \frac{40000}{RT}} \frac{S}{V} K_{sp,S^{2-}} (S_{\text{FeS}} - 1) \quad (115)$$

In this expression, the constant A value was calibrated with the experimental results from the present study and Harmandas *et al.*⁴¹. S_{FeS} is the saturation value of iron sulfide defined as Equation (102):, where

$K_{sp,S^{2-}}$ is the solubility limit of iron sulfide in (mol/L)², which can be calculated from Benning *et al.*⁴²:

$$K_{sp,S^{2-}} = 10^{\left(\frac{2848.779}{T}\right) - 6.347} \times K_{hs} \times K_{bs} \quad (116)$$

4.2.3.2 Electrochemical Reactions

The electrochemical reactions are mainly affected by the coverage of the steel surface by the precipitated corrosion product layer. Assuming the surface area coverage is directly proportional to the porosity of the corrosion product layer, the current density of each electrochemical reaction is calculated by:

$$i_j = \varepsilon \times i_{o,j} \times 10^{\pm \frac{E-E_o}{b_j}} \quad (117)$$

Based on the change in the current density, the flux $N_{out,j}$ at the steel surface can be calculated.

4.2.3.3 Mass Transfer Process

The governing equations used to quantify the mass transfer process for the different species are the same as described in section 4.2.2. The key change is in the mass transfer coefficients for the transport through the porous corrosion product layer, i.e., the diffusion retardation effect. This effect depends on the morphology of the corrosion product layer, such as the thickness, porosity and tortuosity of the layer. Considering the models available in the literature ⁴³⁻⁴⁶, the mass transfer coefficient $k_{s,j}$ through the corrosion product layer is selected as a function of the diffusion coefficient (D_j), porosity (ε), tortuosity (τ) and thickness (δ_s) of the corrosion product layer.

$$k_{s,j} = \frac{\varepsilon \tau D_j}{\delta_s} \quad (118)$$

Here, τ tortuosity is set to be square root of porosity, in an analogy with the theory of porous electrodes ⁴⁷. Only the precipitation of corrosion product in the surface water layer was considered, while the increment in corrosion product layer thickness δ_s is calculated as follows for the two distinct cases:

- when iron carbonate layer forms:

$$\Delta\delta_s = \frac{\Delta x R_{FeCO_3(s)} M_{FeCO_3} \Delta t}{\rho_{FeCO_3}(1 - \varepsilon)} \quad (119)$$

- when iron sulfide layer forms:

$$\Delta\delta_s = \frac{\Delta x R_{FeS(s)} M_{FeS} \Delta t}{\rho_{FeS}(1 - \varepsilon)} \quad (120)$$

Here M_{FeS} and M_{FeCO_3} represent the molecular weight of iron sulfide and iron carbonate (kg/mol); Δt is the time step; ρ_{FeS} and ρ_{FeCO_3} are the density of iron sulfide and iron carbonate (kg/m³).

Substituting the flux density due to mass transfer through corrosion product layer and electrochemical reactions on the steel surface, the mass conservation equation for species j at the steel surface covered by the porous corrosion product layer can be found:

- for the minor species:

$$\Delta x \frac{\partial \varepsilon c_{surface,j}}{\partial t} = -\frac{i_j}{n_j F} + k_{s,j} * (c_{scale,j} - c_{surface,j}) + \Delta x * R_j \quad (121)$$

- for the major species:

$$\Delta x \frac{\partial \varepsilon c_{surface,j}}{\partial t} = k_{s,j} * (c_{scale,j} - c_{surface,j}) + k_{s,j} * \frac{z_j F}{RT} c_{bulk,j} \Delta \Phi_s \quad (122)$$

where $\Delta \Phi_s$ is the potential gradient throughout the porous corrosion product layer.

The mass conservation equations for the bulk of the corrosion product surface water layer is given:

- for the minor species:

$$\begin{aligned} \Delta x \frac{\partial C_{scale,j}}{\partial t} = & -k_{s,j} * (c_{scale,j} - c_{surface,j}) + k_{m,j} \\ & * (c_{bulk,j} - c_{scale,j}) + \Delta x * R_j \end{aligned} \quad (123)$$

for the major species:

$$\Delta x \frac{\partial c_{scale,j}}{\partial t} = -k_{s,j} * (c_{scale,j} - c_{surface,j}) + k_{m,j} * (c_{bulk,j} - c_{scale,j}) \quad (124)$$

$$-k_{s,j} * \frac{z_j F}{RT} c_{bulk,j} \Delta\Phi_s + k_{m,j} * \frac{z_j F}{RT} c_{bulk,j} \Delta\Phi_m$$

where subscript *scale* refers to the corrosion product layer, and $\Delta\Phi_m$ is the potential gradient throughout the corrosion product layer.

Two more electro-neutrality equations for the solution at the steel surface and the corrosion product layer are also needed.

Using the same numerical techniques as introduced in section 4.2.2., all 26 equations can be solved at the same time if porosity ε at the surface water layer is known. Here porosity ε is calculated explicitly by a corrosion product layer growth model developed by Nesic *et al.*⁴⁸, as shown in Equation (125) and Equation (126). The details of these equations are explained in the original paper and will not be repeated here.

for iron carbonate layer:

$$\frac{\partial \varepsilon}{\partial t} = -\frac{M_{FeCO_3}}{\rho_{FeCO_3}} R_{FeCO_3} - CR \frac{\partial \varepsilon}{\partial x} \quad (125)$$

for iron sulfide layer:

$$\frac{\partial \varepsilon}{\partial t} = -\frac{M_{FeS}}{\rho_{FeS}} R_{FeS} - CR \frac{\partial \varepsilon}{\partial x} \quad (126)$$

Here M_{FeCO_3} and ρ_{FeCO_3} are the molecular weight and density of iron carbonate respectively. M_{FeS} and ρ_{FeS} are the molecular weight and density of iron sulfide, respectively. CR represents the corrosion rate in SI units, ε is the porosity.

Since the corrosion process continuously creates voids underneath the corrosion product layer, ε is taken to be close to 1 at the interface between corrosion product layer

and steel surface. Actually the porosity was set as 0.99 to reflect the presence of the iron carbide network emerging from the mild steel (this number can be changed according to the amount of cementite in the steel). Equation (125) and Equation (126) become:

$$\frac{\partial \varepsilon}{\partial t} = -\frac{M_{FeCO_3(S)}}{\rho_{FeCO_3(S)}} R_{FeCO_3(S)} + CR \frac{1-\varepsilon}{\Delta x} \quad (127)$$

$$\frac{\partial \varepsilon}{\partial t} = -\frac{M_{FeS(S)}}{\rho_{FeS(S)}} R_{FeS(S)} + CR \frac{1-\varepsilon}{\Delta x} \quad (128)$$

The procedure for calculation of ε in this model is as follows.

- First, the initial corrosion rate, including surface water chemistry, is determined by the electrochemical corrosion model without the corrosion product layer present.
- Then, a corrosion product prediction model based on thermodynamic framework is used to determine whether a corrosion product layer forms on the steel surface. If a corrosion product layer doesn't form, the calculation is over. If a corrosion product layer forms, a corrosion product layer growth model is invoked.
- The porosity for the corrosion product layer is calculated from Equation (127) or Equation (128), and the thickness of layer is obtained from Equation (120) or Equation (119) depending on which corrosion products forms.
- Finally, the mass conservation equations for each species are solved. Therefore, the concentration for all the chemical species in both the surface water layer and the porous corrosion product layer surface water layer can be obtained.

- The corrosion current, corrosion potential, corrosion rate, potential gradient and the rates (currents) for each of the cathodic reactions and the anodic reaction are calculated.

4.3 Model Verification

4.3.1 Verification of Model without Corrosion Product Layer

Figure 42 shows the comparisons of the model predictions with experiments conducted in a glass cell at flowing conditions using a RCE at 1000 rpm rotating speed. Predictions are in the range of the variation of experimental data, which indicates the model is capable of simulating the kinetics of iron carbonate layer growth and its effect on the corrosion process.

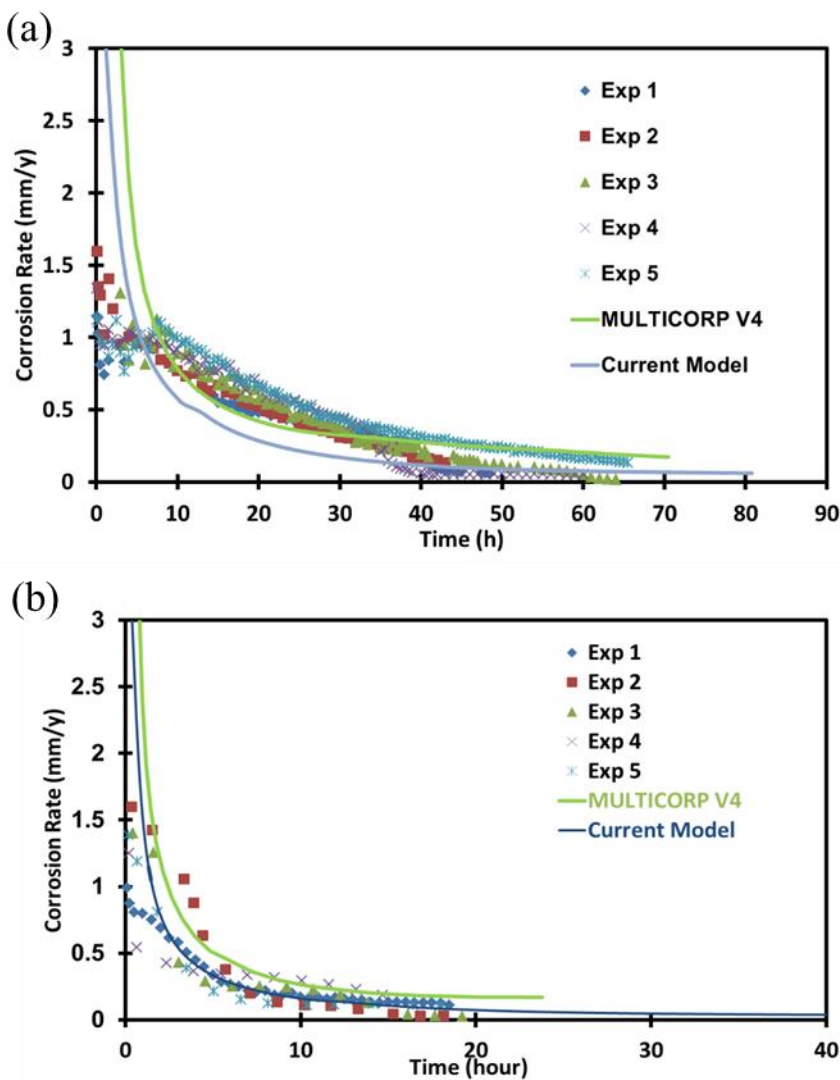


Figure 42. Comparisons between the model predictions and the experiment results for iron carbonate layer forming condition at pH 6.6, 80°C, 0.53 bar CO_2 , and 1000rpm rotating speed, (a) 10 ppm bulk Fe^{2+} , (b) 50 ppm bulk Fe^{2+} .

4.3.2 Verification of Model in Iron Sulfide Layer Forming Conditions

4.3.2.1 Effect of pH_2S

The partial pressure of H_2S , which directly relates to the H_2S concentration in the solution, is an important factor that contributes not only the increase of direct H_2S reduction rate, but also to the iron sulfide layer formation. H_2S plays dual roles here.

First, H₂S is a corrosive species accelerating the corrosion rate by enhancing the cathodic reaction rate. Second, H₂S also promotes the rate of the iron sulfide precipitation that decreases the general corrosion rate.

First, the condition at low partial pressures of H₂S was examined. The test was conducted by Sun ³¹ at H₂S gas partial pressures from 0.54 mbar to 54 mbar. Figure 43 shows that FREECORP™ 2.0 captures the corrosion rate change well.

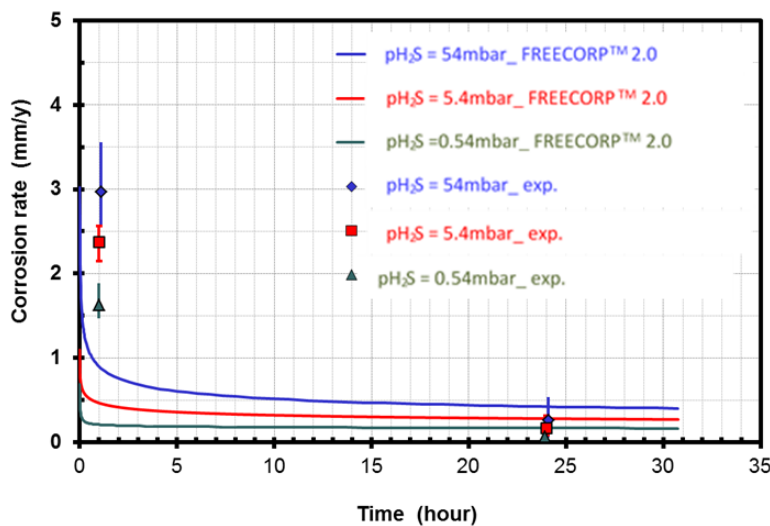


Figure 43. Corrosion rate changing with time at different H₂S partial pressure from current model; points: experimental data, lines: model predictions; conditions: total pressure = 1 bar, H₂S gas partial pressure from 0.54 mbar to 54 mbar, 80°C, experiment duration 1 h to 24 h, pH 5.0 to 5.5, stagnant. Experimental data taken from Sun ³².

Corrosion experiments at higher pH₂S (pH₂S= 16.1 bar in the mixed H₂S/N₂ environment) were reported by Liu ⁴⁹ and FREECORP™ 2.0 predictions are compared

with both the experimental results and FREECORP 1.0 in Figure 44. FREECORPTM 2.0 performs much better than FREECORP 1.0 at this condition.

A similar range of H₂S partial pressures were reported by Bich, *et al.*²⁸ with the main difference being the presence of CO₂. Figure 45 shows the comparison between the model prediction and experimental results in a mixed H₂S/CO₂ environment. FREECORPTM 2.0 captures the corrosion rate change with time, but FREECORP 1.0 tends to over predict the corrosion rate.

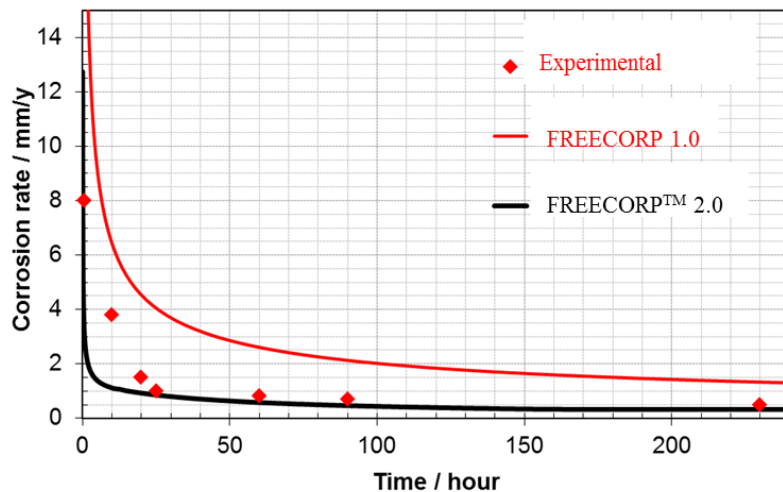


Figure 44. Corrosion rate changing with time, points: experimental data, lines: model predictions; conditions: 16.1 bar H₂S, 90°C, 2L autoclave, stagnant. Experimental data taken from Liu, *et al.*⁴⁹.

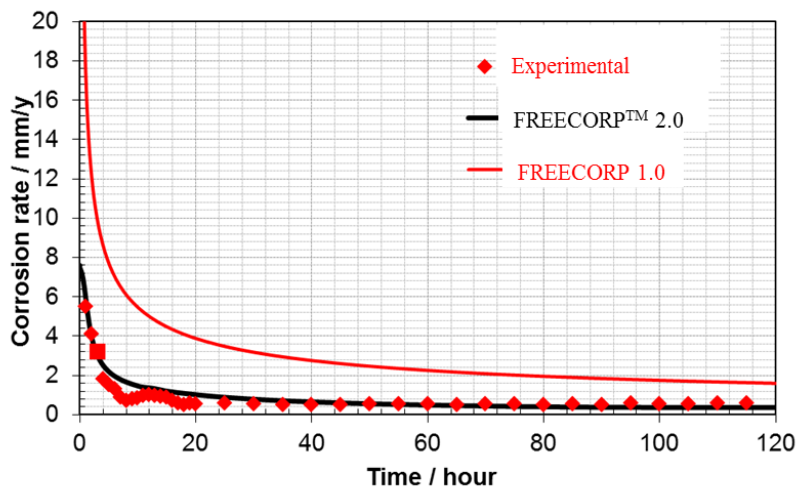


Figure 45. Corrosion rate changing with time, experimental data = points, model predictions = lines; conditions: 12.2 bar H₂S, 3.5 bar CO₂, 65°C. Experimental data taken from Bich *et al.*²⁸

4.3.2.2 Effect of pH

The solution pH is the measurement of the concentration of the free hydrogen ions. These free hydrogen ions accelerate the cathodic reaction by providing more cathodic reaction species. Another significance of the concentration of hydrogen ions is their influence on the formation of the iron sulfide corrosion product layer by affecting the saturation value (S_{FeS}). A higher pH indicates a lower hydrogen ion concentration, so both HS⁻ and S²⁻ concentrations will be higher at the constant concentration of aqueous H₂S. This increases the formation rate of iron sulfide layer and decreases the corrosion rate.

Comparisons between model predictions and experimental results are shown in Figure 46. FREECORP™ 2.0 captures the corrosion rate change much better than FREECORP 1.0. The experimental LPR corrosion rates are much higher than the model prediction at pH 4.0. This is probably due to the iron carbide remaining on the metal surface from corrosion at pH 4.0, which can accelerate the corrosion rate by providing a

more cathodic reaction area^{50, 51}. This effect is not properly included in FREECORPTM 2.0.

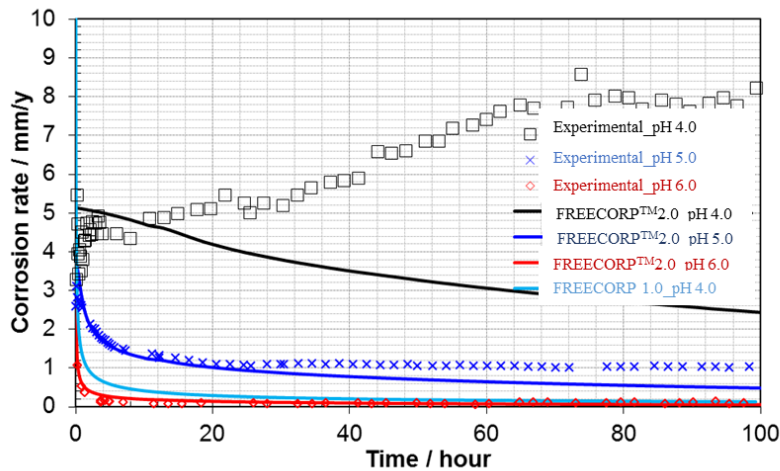


Figure 46. Corrosion rate changing with time, points: experimental data, lines: model predictions; conditions: 0.054 bar pH₂S, balance nitrogen, T = 80°C, stirring rate: 600 rpm.

4.3.2.3 Effect of Flow

Fluid flow and turbulence play an important role in the corrosion process. First, higher flow can increase the corrosion rate through enhancing the mass transport of corrosive species, especially when there is no corrosion product layer formed. Second, flow can also affect the formation of the protective iron sulfide layer. Species transport in turbulent flow affects the surface concentration of species and, consequently, changing the precipitation rate of iron carbonate and iron sulfide.

Figure 47 shows the comparisons between model predictions and experimental results at different stirring rates (i.e. flow velocities). FREECORPTM 2.0 is generally able to predict the change of the corrosion rate with the different stirring rates.

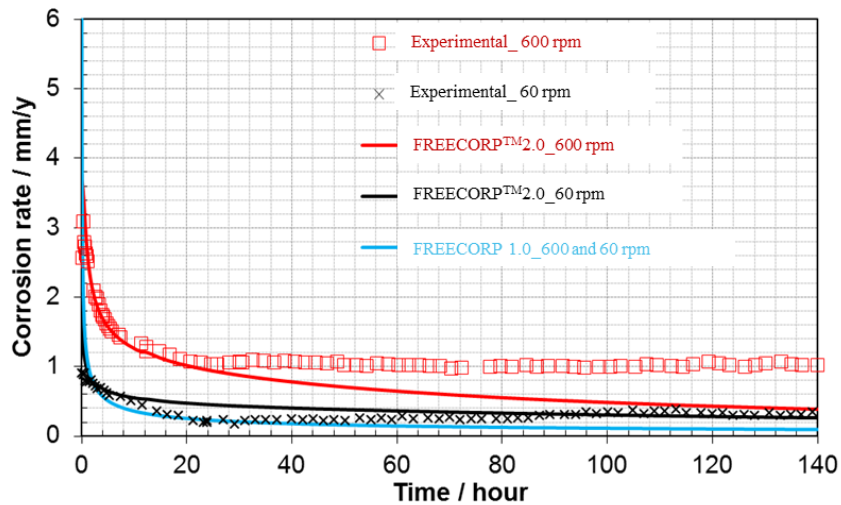


Figure 47. Corrosion rate vs. time, points: experimental data, lines: model predictions; conditions: $\text{pH}_2\text{S} = 0.54 \text{ bar}$, balance N_2 , $T=80 \text{ }^\circ\text{C}$, $\text{pH} 5.0$.

4.3.2.4 Effect of Temperature

Comparisons between model predictions and experimental results at different temperatures are shown in Figure 48 and Figure 49. FREECORP™ 2.0 predicted the corrosion rate much better than FREECORP 1.0 in most cases.

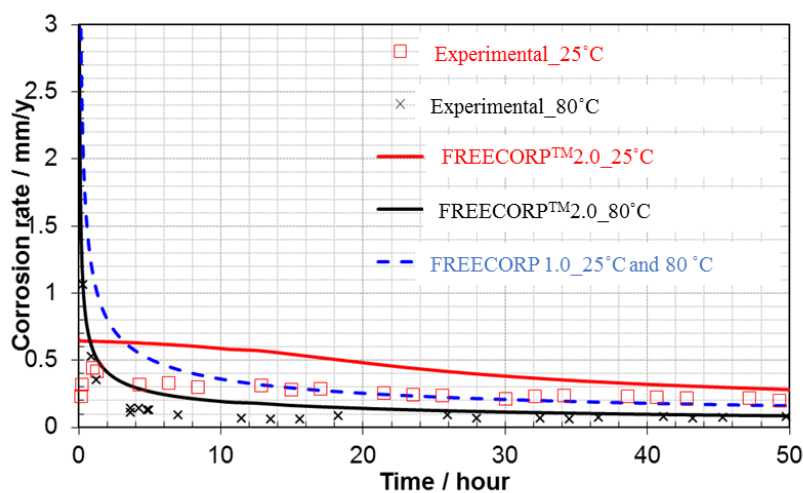


Figure 48. Corrosion rate vs. time, points: experimental data, lines: model predictions; conditions: $\text{pH}_2\text{S} = 0.54$ bar, pH 6.0, 400 rpm stirring rate. Experimental data taken from Ning⁵².

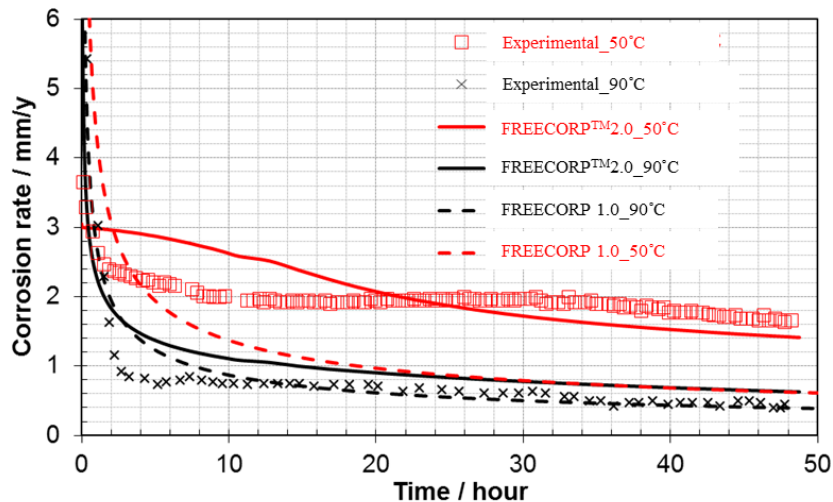


Figure 49. Corrosion rate vs. time, points: experimental data, lines: model predictions; conditions: total pressure= 1 bar, $\text{pH}_2\text{S}=0.3$ bar at 90 °C, $\text{pH}_2\text{S}=0.88$ bar at 50 °C pH 4.2-4.7, Stirring condition. Experimental data taken from Abayarathna, *et al.*²⁷

4.4 Model Limitations

In the transient corrosion model that accounts for formation of corrosion product layers, there are a number of factors which are not taken into consideration. These limitation need to be pointed out here, to avoid the misuse of FREECORP™ 2.0. Major limitations of transient corrosion model are listed below:

- The model covers only uniform carbon steel corrosion. It does not address localized corrosion, even if it forms a solid foundation for constructing a localized corrosion model.
- A simple water chemistry was considered, which means that the infinite solution theory and an ideal solution are assumed. Concentrations of different species are

used rather than activities. This can be changed with implementation of a model for non-ideal solution chemistry.

- Empirical mass transfer correlations are used to account for the mass transfer process, making it only take into account the effect of single-phase pipe flow. However, empirical mass transfer correlations for different flow geometries as well as for multiphase flow can be coupled readily implemented.
- The effects of high salt concentration, oxygen, elemental sulfur on the corrosion process are not considered.
- Mackinawite is the only type of iron sulfide corrosion product considered in FREECORPTM 2.0. The various transformations of mackinawite to other type of iron sulfides are known to happen over time, and this is not included in the model. However, when the kinetics of precipitation and transformations to other types of iron sulfides are available, the new physics can be added to the current mechanistic corrosion model.
- FREECORPTM 2.0 does not account for the effect of iron carbide on the corrosion.
- The chemical processes are only considered in the bulk solution and at the steel surface. FREECORPTM 2.0 ignores the chemical processes though the boundary layer.

REFERENCES

1. Nesic, S., Postlethwaite, J. & Olsen, S. An electrochemical model for prediction of corrosion of mild steel in aqueous carbon dioxide solutions. *Corrosion* **52**, 280–

- 294 (1996).
2. Gray, L. G. S., Anderson, B. G., Danysh, M. J. & Tremaine, P. R. Effect of pH and temperature on the mechanism of carbon steel corrosion by aqueous carbon dioxide. in *CORROSION/90* (Houston TX: NACE, 1990).
 3. de Waard, C. & Milliams, D. E. Carbonic acid corrosion of steel. *Corrosion* **31**, 177–181 (1975).
 4. Oddo, J. E. & Tomson, M. B. Simplified calculation of CaCO_3 saturation at high temperatures and pressures in brine solutions. *J. Pet. Technol.* **34**, 1583–1590 (1982).
 5. Palmer, D. A. & Van Eldik, R. The chemistry of metal carbonate and carbon dioxide complexes. *Chem. Rev.* **83**, 651–731 (1983).
 6. Kharaka, Y. K., Gunter, W. D., Aggarwal, P. K., Perkins, E. H. & Dedraal, J. D. *SOLMINEQ. 88: A computer program for geochemical modeling of water - rock interactions.* (Alberta Research Council, 1988).
 7. Nesic, S. Key issues related to modelling of internal corrosion of oil and gas pipelines: a review. *Corros. Sci.* **49**, 4308–4338 (2007).
 8. Ning, J., Zheng, Y., Young, D., Brown, B. & Nešić, S. Thermodynamic study of hydrogen sulfide corrosion of mild steel. *Corrosion* **70**, 375–389 (2014).
 9. Suleimenov, O. M. & Krupp, R. E. Solubility of hydrogen sulfide in pure water and in NaCl solutions, from 20 to 320 °C and at saturation pressures. *Geochim. Cosmochim. Acta* **58**, 2433–2444 (1994).
 10. Bockris, J. O., Drazic, D. & Despic, A. R. The electrode kinetics of the deposition and dissolution of iron. *Electrochim. Acta* **4**, 325–361 (1961).

11. Nordsveen, M., Nesic, S., Nyborg, N. & Stangeland, A. A mechanistic model for carbon dioxide corrosion of mild steel in the presence of protective iron carbonate films part 1: theory and verification. *Corrosion* **59**, 433–456 (2003).
12. Eisenberg, M., Tobias, C. W. & Wilke, C. R. Ionic mass transfer and concentration polarization at rotating electrodes. *J. Electrochem. Soc.* **101**, 306–320 (1954).
13. Berger, F. P. & Hau, K.-F. F.-L. Mass transfer in turbulent pipe flow measured by the electrochemical method. *Int. J. Heat Mass Transf.* **20**, 1185–1194 (1977).
14. Atkins, P. W. *Physical Chemistry*. (Oxford University Press, 1982).
15. Weast, R. C. *Handbook of Chemistry & Physics*. (CRC Press Inc., 1985).
16. Nesic, S., Pots, B. F. M., Postlethwaite, J. & Thevenot, N. Superposition of diffusion and chemical reaction controlled limiting currents—application to CO₂ corrosion. *J. Corros. Sci. Eng.* **1**, (1995).
17. Rickard, D. & Luther, G. W. *Chemistry of iron sulfides*. *Chemical reviews* **107**, (2007).
18. Kittel, J., Ropital, F., Grosjean, F., Sutter, E. M. M. & Tribollet, B. Corrosion mechanisms in aqueous solutions containing dissolved H₂S. part 1: characterisation of H₂S reduction on a 316l rotating disc electrode. *Corros. Sci.* **66**, 324–329 (2013).
19. Morris, D. R., Sampaleanu, L. P. & Veysey, D. N. The corrosion of steel by aqueous solutions of hydrogen sulfide. *J. Electrochem. Soc.* **127**, 1228–1235 (1980).
20. Cheng, X. L. *et al.* Corrosion of iron in acid solutions with hydrogen sulfide. *Corrosion* **54**, 369–376 (1998).

21. Perry, R. H. & Green, D. W. *Perry's chemical engineers' handbook*. (McGraw-Hill, 1997).
22. Ma, H. *et al.* The influence of hydrogen sulfide on corrosion of iron under different conditions. *Corros. Sci.* **42**, 1669–1683 (2000).
23. Zheng, Y., Brown, B. & Nešić, S. Electrochemical Study and Modeling of H₂S Corrosion of Mild Steel. **70**, 351–365 (2014).
24. A. Kahyarian, B. Bruce, and S. Nesic, “ Mechanism of Cathodic Reactions in Acetic Acid Corrosion of Iron and Mild Steel,” *Corrosion*, (2016) [.http://dx.doi.org/10.5006/2177](http://dx.doi.org/10.5006/2177).
25. Lee, K. L. J. A mechanistic modeling of CO₂ corrosion of mild steel in the presence of H₂S. (Ohio University, 2004).
26. Choi, Y.-S., Nesic, S. & Ling, S. Effect of H₂S on the CO₂ corrosion of carbon steel in acidic solutions. *Electrochim. Acta* **56**, 1752–1760 (2011).
27. Abayarathna, D., Naraghi, A. R. & Wang, S. The effect of surface films on corrosion of carbon steel in a CO₂-H₂S-H₂O system. in *CORROSION/2005* (Houston, TX: NACE, 2005).
28. Bich, N. N. & Goerz, K. G. Caroline pipeline failure: findings on corrosion mechanisms in wet sour gas systems containing significant CO₂. in *CORROSION/96* (Houston, TX: NACE, 1996).
29. Omar, I. H., Gunaltun, Y. M., Kvarekval, J. & Dugstad, A. H₂S corrosion of carbon steel under simulated kashagan field conditions. in *CORROSION/2005* (Houston, TX: NACE, 2005).
30. Y. Sun, K. George, S. Nešić, “The Effect of Cl⁻ and Acetic Acid on Localized CO₂

Corrosion in Wet Gas Flow", CORROSION/2003, Paper No. 3327, (Houston, TX: NACE International 2003).

31. Sun, W. & Nesic, S. A Mechanistic Model of Uniform Hydrogen Sulfide / Carbon Dioxide Corrosion of Mild Steel. **65**, 291–307 (2009).
32. W. Sun, S. Nesic, and R. C. Woollam, "The effect of temperature and ionic strength on iron carbonate (FeCO_3) solubility limit," Corrosion Science, vol. 51, pp. 1273-1276, 2009
33. S. Nesic and W. Sun, "Corrosion in Acid Gas Solutions," in Shreir's Corrosion. vol. 2, Amsterdam: Elsevier, pp. 1270-1298, 2010
34. Nesic, S., Stangeland, A., Nordsveen, M. & Nyborg, R. A mechanistic model for carbon dioxide corrosion of mild steel in the presence of protective iron carbonate films part 2: a numerical experiment. *Corrosion* **59**, (2003).
35. Newman, J. S. *Electrochemical Systems*. (Prentice Hall, 1991).
36. Y. Zheng, "Electrochemical mechanism and model of H₂S corrosion of carbon steel," Ph.D. Dissertation, Ohio University, 2015.
37. Pots, B. F. M. Mechanistic models for the prediction of CO₂ corrosion rates under multi-phase flow conditions. in *CORROSION/95* (Houston, TX: NACE, 1995).
38. Tanupabungsun, T. Thermodynamics and kinetics of carbon dioxide corrosion of mild steel at elevated temperatures. (Ohio University, 2012).
39. Sun, W. Kinetics of iron carbonate and iron sulfide scale formation in carbon dioxide/hydrogen sulfide corrosion. (Ohio University, 2006).
40. Rickard, D. Kinetics of FeS precipitation: part 1. competing reaction mechanisms. *Geochim. Cosmochim. Acta* **59**, 4367–4379 (1995).

41. Harmandas, N. G. & Koutsoukos, P. G. The formation of iron(II) sulfides in aqueous solutions. *J. Cryst. Growth* **167**, 719–724 (1996).
42. Benning, L. G., Wilkin, R. T. & Barnes, H. L. Reaction pathways in the FeS system below 100 °C. *Chem. Geol.* **167**, 25–51 (2000).
43. Cussler, E. L. *Diffusion: mass transfer in fluid systems*. (Cambridge University Press, 1997).
44. Grathwohl, P. *Diffusion in natural porous media: contaminant transport, sorption/desorption and dissolution kinetics*. (Springer US, 1998).
45. Gopal, M., Rajappa, S. & Zhang, R. Modeling the diffusion effects through the iron carbonate layer in the carbon dioxide corrosion of carbon steel. in *CORROSION/98* (Houston TX: NACE, 1998).
46. Mu, D., Liu, Z.-S., Huang, C. & Djilali, N. Determination of the effective diffusion coefficient in porous media including knudsen effects. *Microfluid. Nanofluidics* **4**, 257–260 (2008).
47. Pisani, L. Simple expression for the tortuosity of porous media. *Transp. Porous Media* **88**, 193–203 (2011).
48. Nesic, S. & Lee, K. L. J. A mechanistic model for carbon dioxide corrosion of mild steel in the presence of protective iron carbonate films part 3: film growth model. *Corrosion* **59**, 616–628 (2003).
49. Liu, M., Wang, J., Ke, W. & Han, E.-H. Corrosion behavior of X52 anti-H₂S pipeline steel exposed to high H₂S concentration solutions at 90 °C. *J. Mater. Sci. Technol.* **In press**,
50. Farelas, F., Brown, B. & Nesic, S. Iron carbide and its influence on the formation

of protective iron carbonate in CO₂ corrosion of mild steel. in *CORROSION/2013*

(Houston TX: NACE, 2013).

51. Berntsen, T., Seiersten, M. & Hemmingsen, T. Effect of FeCO₃ supersaturation and carbide exposure on the CO₂ corrosion rate of carbon steel. *Corrosion* **69**, 601–613 (2013).
- 52 Ning, J. Investigation of polymorphous iron sulfide in H₂S corrosion of mild steel. in (Ohio Univesity, 2013).